AFRL-AFOSR-UK-TR-2019-0016

Boundary Layer Establishment and Separation: Discovering the Dynamic Scales

Guillermo Paniagua
INSTITUT VON KARMAN DE DYNAMIQUE DES FLUIDES VZW
WATERLOOSESTEENWEG 72
SINT-GENESIUS-RODE, 1640
BE

03/19/2019
Final Report

Air Force Research Laboratory
Air Force Office of Scientific Research
European Office of Aerospace Research and Development
Unit 4515 Box 14, APO AE 09421

REPORT DOCUMENTATION PAGE

Form Approved
OMB No. 0704-0188

1. REPORT DATE *(DD-MM-YYYY)*	2. REPORT TYPE	3. DATES COVERED *(From - To)*
19-03-2019	Final	01 Dec 2015 to 30 Nov 2018

4. TITLE AND SUBTITLE
Boundary Layer Establishment and Separation: Discovering the Dynamic Scales

5a. CONTRACT NUMBER

5b. GRANT NUMBER
FA9550-16-1-0120

5c. PROGRAM ELEMENT NUMBER
61102F

6. AUTHOR(S)
Guillermo Paniagua

5d. PROJECT NUMBER

5e. TASK NUMBER

5f. WORK UNIT NUMBER

7. PERFORMING ORGANIZATION NAME(S) AND ADDRESS(ES)
INSTITUT VON KARMAN DE DYNAMIQUE DES FLUIDES VZW
WATERLOOSESTEENWEG 72
SINT-GENESIUS-RODE, 1640 BE

8. PERFORMING ORGANIZATION REPORT NUMBER

9. SPONSORING/MONITORING AGENCY NAME(S) AND ADDRESS(ES)
EOARD
Unit 4515
APO AE 09421-4515

10. SPONSOR/MONITOR'S ACRONYM(S)
AFRL/AFOSR IOE

11. SPONSOR/MONITOR'S REPORT NUMBER(S)
AFRL-AFOSR-UK-TR-2019-0016

12. DISTRIBUTION/AVAILABILITY STATEMENT
A DISTRIBUTION UNLIMITED: PB Public Release

13. SUPPLEMENTARY NOTES

14. ABSTRACT
The dynamic performance of the momentum and thermal boundary layer linked to the acoustic response dictate the efficiency of heat exchangers and the operational limits of fluid machinery. The specific time required by the boundary layer to establish or adapt
to the free stream variations is vital to optimize flow control strategies as well as the thermal management of fluid systems. The proper understanding of the wall fluxes, separated flow regions and free stream response to transient conditions becomes the fulcrum of the further improvement of fluid machinery performance and endurance. Throughout this dissertation the establishment sequence and the main parameters dictating the acoustic response and the boundary layer settlement are quantified together with
their implication on the wall fluxes and boundary layer detachment.
Unsteady Reynolds Average Navier Stokes evaluations, Large Eddy Simulations, Direct Numerical Simulations and wind tunnel experiments are exploited to analyze the transient behavior of attached and detached flow aerodynamics. The core of the research is
built upon URANS simulations allowing the realization of multiple detailed parametric analyses. Thanks to its reduced

15. SUBJECT TERMS
EOARD, Boundary Layer Dynamic Scales

16. SECURITY CLASSIFICATION OF:			17. LIMITATION OF ABSTRACT	18. NUMBER OF PAGES	19a. NAME OF RESPONSIBLE PERSON
a. REPORT	b. ABSTRACT	c. THIS PAGE			SMITH, DOUGLAS
Unclassified	Unclassified	Unclassified	SAR		19b. TELEPHONE NUMBER *(Include area code)* 314-235-6013

von Karman Institute for Fluid Dynamics
Purdue University

Boundary Layer Establishment and Separation: Discovering the Dynamic Scales

FA-9550-16-1-0120

Guillermo Paniagua
Jorge Saavedra

01 DEC 2015 - 30 NOV 2018

Table of Contents

List of Figures

List of Tables

Summary

The dynamic performance of the momentum and thermal boundary layer linked to the acoustic response dictate the efficiency of heat exchangers and the operational limits of fluid machinery. The specific time required by the boundary layer to establish or adapt to the free stream variations is vital to optimize flow control strategies as well as the thermal management of fluid systems. The proper understanding of the wall fluxes, separated flow regions and free stream response to transient conditions becomes the fulcrum of the further improvement of fluid machinery performance and endurance. Throughout this dissertation the establishment sequence and the main parameters dictating the acoustic response and the boundary layer settlement are quantified together with their implication on the wall fluxes and boundary layer detachment.

Unsteady Reynolds Average Navier Stokes evaluations, Large Eddy Simulations, Direct Numerical Simulations and wind tunnel experiments are exploited to analyze the transient behavior of attached and detached flow aerodynamics. The core of the research is built upon URANS simulations allowing the realization of multiple detailed parametric analyses. Thanks to its reduced computational cost, hundreds of transient flow evaluations are carried out, enabling the determination of the establishment sequence, the main flow features and relevant non-dimensional numbers. The URANS methodology is verified against experimental and analytic results on the flow conditions of the study. The Large Eddy Simulations and Direct Numerical Simulations allow further characterization of the near wall flow region behavior with much higher resolution while providing an additional source of verification for the coarser numerical tools. An experimental campaign on a novel full visual access linear wind tunnel explores the impact of mean flow sudden accelerations on the boundary layer detachment and reattachment phenomena over an ad-hoc wall mounted hump. The wind tunnel is designed based on the premises of: full visual access, spatial and temporal stability of total and static pressure together with the total temperature and fast flow settlement, minimizing the start-up phase duration of the wind tunnel. A wall mounted hump that mimics the behavior of the aft portion of a low pressure turbine is inserted in the wind tunnel guaranteeing a 2D flow separation phenomena. After steady state test article characterization series of sudden flow discharge experiments reveal the impact of mean flow transients on the boundary layer detachment inception. Finally, taking advantage of the knowledge on transient flow performance, optimum flow control mechanisms to abate boundary layer detachment are proposed. The recommended control approach effectively prevents the boundary layer separation while minimizing the energy requirement.

Introduction

Many vital components of fluid mechanic machinery operate under transient mean flow conditions dictated by their operating regime. Traditionally their performance is analyzed based on steady-state operation. However, in an evolution towards new levels of performance and efficiency, researchers have found that the transient operation of fluid machinery is one of the main areas that still requires more characterization.

The boundary layer transient growth was previously documented in fundamental and analytical studies of for laminar flow conditions. Several authors proposed numerical solutions of the unsteady boundary layer development. Stewartson [1, 2] studied the impulsive start of motion of semi-infinite flat plates. Rott [3] also looked into the theory of time dependent laminar flows, describing the evolution of laminar boundary layers driven by free-stream flow changes. In a similar analysis, Moore [4] carried a dimensionless evaluation of the flow establishment over a flat plate. The response of the boundary layer to mean flow changes is dictated by the diffusion across its height. Starting from the exact solution of the Navier-Stokes equations for 2-D incompressible laminar flow, Watson derived a model that could predict the skin friction establishment time. Theoretically, Wen and Huang [5] highlighted the prime role of the acceleration rate on the boundary layer transient evolution.

Schetz and Oh [6] analyzed the transient development of the near wall flow region driven by the impulsive start of motion of the surrounding fluid. Taking advantage of the unsteady momentum integral equations and using an ad-hoc boundary layer profile with the Howarth-Dorodnitzin transformation and Crocco Integral relations they predicted the momentum and thermal boundary layer evolution.

Most of the heat transfer, supersonic and hypersonic research in aerospace components is empirically evaluated in short-duration wind tunnels. Their use is optimal for this application due to the large temperature gradient that can be instantaneously imposed between the flow and the test article, enabling high accuracy measurements. On the other hand, the test duration is generally constrained to a few milliseconds due to the demanding upstream flow conditions required for the experimental operation. In sudden flow release wind tunnels, the flow is set into motion following a rapid valve opening or diaphragm burst causing pressure waves to travel across the test section. Mirels [7, 8] analyzed the boundary layer growth during the flow start-up after the passage of a shock-wave. Similarly, Holden [9, 10] experimentally studied the flow establishment of flows in the supersonic regime, describing that the time to reach steady state is a function of the flow speed, Reynolds number, Mach number and the gas to wall temperature ratio. In this line, Lewis [11] performed numerical evaluations that agreed with Holden's model and provided predictions of the boundary layer development time. Also experimentally, Davies [12] described the formation of a shock-induced boundary layer on a semi-infinite flat plate. Focusing on the starting phase of sudden flow release wind tunnels, Smith [13] studied the starting process in a reflected shock tunnel. In their experiments a relation between the mean flow evolution and the boundary layer transient development was clearly exposed. In a similar research, Lam & Crocco [14] focused their analysis on the shock induced unsteady laminar compressible boundary layer on a flat plate.

In the turbulent flow regime, Horlock and Evans [15] analyzed the influence of turbulence and ordered unsteadiness in the free-stream on the boundary layer development. Additional terms related to the shear stress and the kinetic energy in the edge of the boundary layer appeared to be of relevance on the 2D momentum integral equations. The turbulent kinetic energy and shear stress at the boundary layer edge must be considered in order to capture the influence of such transient turbulent structures on the near wall region. In this line, low-order models were also applied to model the low-frequency motions observed in reflected shock-wave boundary layer interactions by Touber & Sandham [16], using results of direct numerical simulation to determine the relevant parameters from the 3-D momentum integral equations. In attempt to predict the turbulent boundary layer establishment time Saavedra et al. performed and extensive parametric analysis on the development of the boundary layer under sudden flow discharge based on URANS blowdown simulations [17]. Through the isolation of the independent effect of each one of the driver parameters a correlation was derived to predict the boundary layer establishment time.

Many analysis have been carried out in turbomachinery flows to uncover the effect of wake impingement on downstream components [18] [19] [20] [21]. In particular, Moss et al. [22] experimentally described the heat transfer along the suction and pressure side of turbine rotor airfoils in a rotating annular facility with and without stator vanes. The effect of the impinging wakes on the heat flux along the rotor blade was highlighted, comparing the results of stator and stator-less experiments. Thoroughly different heat flux evolutions were described in the rear suction side blade driven by the presence of the stator wakes. In this regard, as new combustion approaches are explored for propulsion concepts, like pulse detonation or rotating detonation combustors [23], new fluid machinery components are developed [24],[25]. The performance of such units under pulsating conditions becomes a fulcrum for future technology integration. Sousa et al [26] described the transient flow behavior experienced across internal flow passages exposed to variable inlet flow conditions in supersonic flow conditions. The impact of transient mean flows with the exhaust propulsive elements requires more understanding to ensure efficient energy usage and optimal performance [27, 28].

In the field of boundary layer response to continuous flow fluctuations, Lighthill carried out analytical studies on the laminar boundary layer reaction to mean flow variations, describing the main differences among subsonic and supersonic mean flow regimes [29] [30]. Adding the energy equation in the methodology, the impact of free-stream and wall temperature temporal evolution enabled the heat transfer rate characterization across laminar incompressible boundary layers [31]. Uchida [32] revealed the influence of the dynamic pressure gradients travelling along the pipe on the wall fluxes on laminar flows. Similarly, Mizushina et al. [33] experimentally characterized the instantaneous profiles of velocity and turbulence intensity for pulsating flows. Based on their empirical investigation, two main regimes were distinguished. At low frequencies the turbulence levels remained unaltered, but the mean flow conditions suffered high variations. In contrast, for higher frequencies, the mean flow quantities were stable while the turbulent characteristics suffered strong oscillations. Regarding the impact of free-stream fluctuations on the wall heat flux, Moschandreou and Zamir [34] depicted the main role of Prandtl and Strouhal number on the heat flux rate oscillation magnitude driven by the free-stream changes. The ratio between the thermal to momentum boundary layer has a strong influence on the heat flux transient evolution, as also analyzed by Saavedra et al [35].

In the present investigation, the authors report a numerical study analyzing the effect of a sudden flow acceleration on the development of the boundary layer. Based on direct numerical simulations (DNS), both the mean properties and integral boundary layer properties are analyzed. Unsteady Reynolds-averaged Navier-Stokes (URANS) calculations are also carried out to evaluate the capability of the kω- Transitional Shear StressTransport (SST) model to capture the influence of mean flow transients on the near wall region and their impact on the wall fluxes distribution.

Detailed simulation on the boundary layer reaction to sudden flow acceleration

In order to verify the dynamic resolution of URANS solver and the turbulence closure selected, a sudden flow acceleration from Mach 0.3 to Mach 0.6 will be compared to the results of a Direct Navier Stokes simulation, [36, 37]. Based on Direct Numerical Simulations (DNS), both the mean properties and integral boundary layer properties are analyzed. Taking advantage of the higher resolution analysis and the 3D boundary layer momentum integral equations a simplified integral model is developed to predict the compressible turbulent boundary layer growth under free-stream transient behavior. Finally, taking advantage of the transient boundary layer development model and current skin friction correlations, the shear stress evolution along the transient can also be estimated.

Description of numerical approach, Methods, Assumptions and Procedures

Numerical Domain

The analysis is focused on a flat plate geometry that allows the extrapolation of the results to a myriad of configurations. Figure 1 depicts the numerical domain for the transient evaluation of the compressible turbulent boundary layer evolution driven by sudden flow acceleration. The total length of the domain (L) was equal to 128.5 times the height of the inlet boundary layer ($\delta_0 = 8$ mm). The global length of the domain determines the acoustic response of the test geometry and constrains the establishment time of the mean flow characteristics. For the Direct Numerical Simulations the finely resolved region ended at 100 δ_0 (L^x), and grid stretching was employed in the remainder of the domain to support the outflow boundary condition (a sponge layer). The total height of the domain (H) was equal to 125 δ_0, ensuring minimal influence of the boundary layer displacement thickness (δ^*) growth on the free-stream velocity, (H >150 δ^*). For the DNS, the mesh was finely resolved till 7 δ_0 (H^x), with grid stretching employed for the rest of the domain in the wall-normal direction. The width of the domain (W) is 28 δ_0. The DNS solutions are averaged across the span wise direction to provide representative 2-D transient conditions throughout the acceleration.

The computational mesh consisted of about 376 million points arranged in a $2026 \times 326 \times 569$ structured mesh. The sponge layers at the top and end of the domain consisted of 25 points, with a stretching factor of 1.2. An overlap layer of 9 points was used to enforce a periodic boundary condition in the spanwise direction. Since the freestream flow conditions varied, so did the non-dimensional grid spacing. For the flow conditions most challenging for numerical accuracy, the grid resolution in the resolved region was $\Delta x^+ = 32$ in the streamwise direction and $\Delta z^+ = 32$ in the spanwise direction. The resolution in the wall-normal direction varied from $\Delta y^+ = 0.7$ at the wall to $\Delta y^+ = 24$ at the boundary layer edge. These parameters correspond to the final boundary layer state; the values for the initial boundary layer state were about half as large. The largest non-dimensional time step for the calculations was about $\Delta t^+ = 0.3$ with an equivalent dimensional time step of 0.5 μs. The DNS were carried out on 4320 cores, with 360 subdomains ($20 \times 3 \times 6$) parallelized using MPI, and with 12 OpenMP threads per MPI rank. Data for computing turbulence statistics were saved every 200 computational steps (every 0.1 ms) for the following planes: $x/\delta_0 = 100$, $y/\delta_0 = 0$, $z/\delta_0 = 14$. For the 10 ms rise time, at total of 198000 time steps (99 ms) were computed, while 300000 time steps (150 ms) were evaluated for the 25 ms rise time.

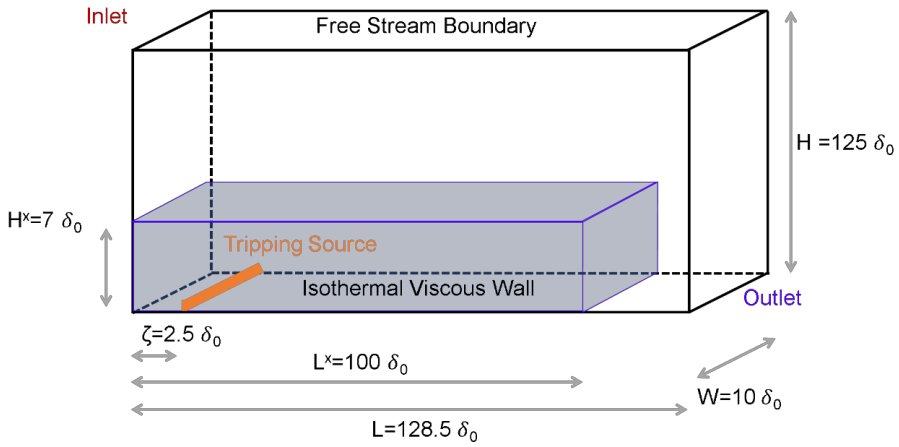

Figure 1: Numerical Domain

Boundary conditions

In order to model the sudden flow acceleration in the numerical domain the static pressure level was fixed at 16 kPa in the outlet, right boundary. The inlet of the domain was modeled as a pressure boundary condition where the total temperature was kept constant at 500K. The free-stream flow acceleration was imposed following total pressure transient profile, $P_0(t)$. The total pressure rise in the inlet was imposed following the "smoother step function" [38] evolution (2.1), as depicted in Figure 2 a). The use of the smoother step function guarantees the continuity of the signal through the pressure rise. For the first 36.4 ms of the simulation, $t < t_0$, the total pressure was set at 17 kPa simulating the steady state conditions for Mach 0.3 flow, where the Reynolds number based on the momentum thickness is 1202 at L^*. Then the total pressure was raised to 20.5 kPa over 10 ms following the smoother step profile. Finally, the total pressure was kept at 20.5 kPa up to t =100 ms to reach steady flow conditions at Mach 0.6. The steady flow conditions at the initial and final status are summarized in Table 1. A second transient acceleration with a rise time of 25 ms was evaluated to explore the impact of the acceleration rate and to verify the accuracy of the developed model. The top wall of the domain was modeled as an adiabatic inviscid wall. (For the DNS, extrapolation was used at the upper boundary.) While the plate was simulated as a viscous isothermal surface at 300 K. A periodic boundary condition was imposed in the spanwise direction for the lateral boundaries of the domain.

$$P_0(t)\begin{cases} 17\ kPa & t < t_0 \\ 17 + 3.5\left(6\left(\frac{t-t_0}{\Delta t}\right)^5 - 15\left(\frac{t-t_0}{\Delta t}\right)^4 + 10\left(\frac{t-t_0}{\Delta t}\right)^3\right) kPa & t_0 < t < t_0 + \Delta t \\ 20.5\ kPa & t > t_0 + \Delta t \end{cases} \quad (2.1)$$

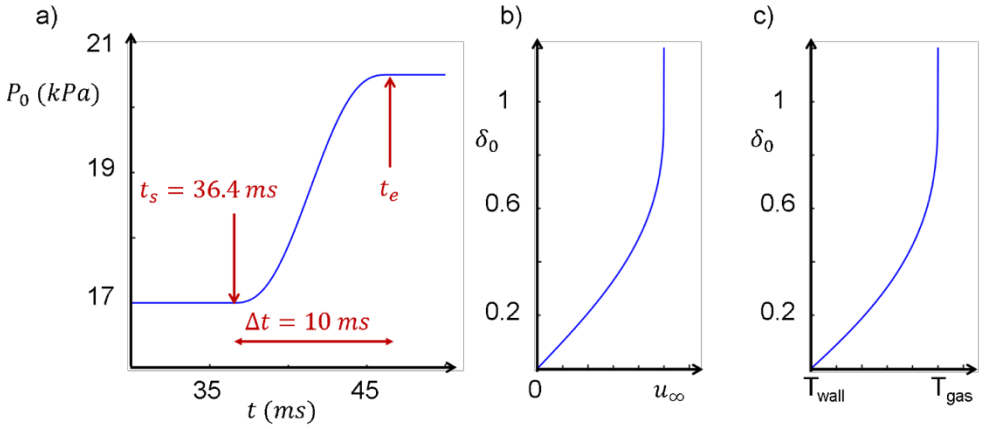

Figure 2: Inlet boundary conditions; a) P_0 transient profile, b) Initial momentum boundary layer, c) Initial thermal boundary layer

An initial laminar boundary layer was imposed at the inlet with a height of 8 mm, δ_0. The momentum boundary layer followed a Polhausen profile, eq. (2.2). Similarly, the thermal boundary layer was derived from the momentum one taking advantage of the Crocco relation for temperature, eq. (2.3). Both momentum and thermal boundary layer are depicted on Figure 2 b) and c) respectively.

$$u = u_\infty \left(2\left(\frac{y}{\delta_0}\right) - 2\left(\frac{y}{\delta_0}\right)^3 + \left(\frac{y}{\delta_0}\right)^4\right) \tag{2.2}$$

$$T = T_{wall} + \left(T_{gas} - T_{wall}\right)\left(\frac{u}{u_\infty}\right) + \frac{1}{2}\sqrt{Pr}\,(\gamma - 1)M^2 T_{gas}\left(\left(\frac{u}{u_\infty}\right) - \left(\frac{u}{u_\infty}\right)^2\right) \tag{2.3}$$

Table 1: Steady Initial and Final flow conditions

	P_0 (kPa)	P (kPa)	T_0 (K)	M	Reθ
Initial Condition	17	16	500	0.2968	1202
Final Condition	20.5	16	500	0.6061	2162

Boundary layer trip

To resolve the impact of the sudden flow acceleration on a fully developed turbulent boundary layer a trip model was employed to promote the transition of the initial laminar boundary layer. The artificial body force term used here was similar to the one used by Mullenix et al. [39] and Bisek et al [40]. A counter-flow body force was applied near the wall, 2.5 δ_0 downstream of the inlet plane. For the RANS computations, the source term imposed a 5 kN body force of with an angle α of 5 degrees over a rectangular region of 1.25 x 0.125 δ_0 cross section. The source term was continuously applied uniformly across the span of the domain, as displayed in Figure 3. For the DNS, the trip had the following form:

$$F = \frac{F_0}{\pi\, x_r y_r} \exp\left[-\left(\frac{x - x_0}{x_r}\right)^2 - \left(\frac{y - y_0}{y_r}\right)^2\right]$$

$$f_x = F\cos\alpha$$

$$f_y = F\sin\alpha$$

Where the non-dimensional values of the parameters are: $F_0 = 0.03$, $x_0 = 2.5$, $x_r = 0.17$, $y_0 = 0$, $y_r = 0.01$, $\alpha = 1°$. The non-dimensional values are based on reference parameters of $\rho_R = 0.11$ kg/m^3, $U_R = 131.9$ m/s, $\delta_0 = 8.0$ mm.

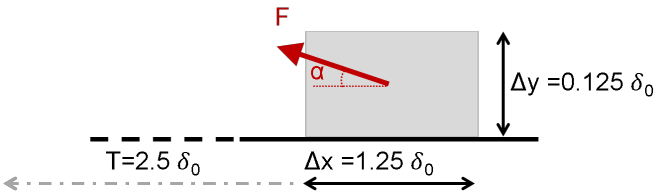

Figure 3: Tripping source term

Solvers

Direct Numerical Simulations

Regarding the numerical solvers, the three-dimensional compressible Navier-Stokes equations are solved directly without modeling using the code HOPS (Higher Order Plasma Solver), developed by the second author [37, 41]. The physical model consists of the perfect-gas, compressible-flow formulation. The conservation of mass, momentum, and energy are formulated as:

$$\frac{\partial \rho}{\partial t} + \frac{\partial}{\partial x_j}\left(\rho u_j\right) = 0 \tag{2.4}$$

$$\frac{\partial}{\partial t}(\rho u_i) + \frac{\partial}{\partial x_j}\left(\rho u_j u_i - \Sigma_{ji}\right) = f_i \tag{2.5}$$

$$\frac{\partial \vartheta}{\partial t} + \frac{\partial}{\partial x_j}\left(u_j \vartheta - \Sigma_{ji} u_i - Q_j\right) = f_i u_i + S \tag{2.6}$$

where ρ is the gas density, u_i is the velocity, Σ_{ij} is the total stress tensor, $\vartheta = \rho(\epsilon + u_k u_k/2)$ is the total energy of the fluid, ϵ is the internal energy and Q_j is the heat flux. The additional terms f_i and S are included to account for optional body force and energy sources.

The total stress tensor Σ_{ij} is given by the constitutive equation for a Newtonial fluid, and the heat flux Q_j follows Fourier's heat conduction law.

$$\Sigma_{ij} = -p\delta_{ij} + \mu\left(\frac{\partial u_i}{\partial x_j} + \frac{\partial u_j}{\partial x_i}\right) - \frac{2}{3}\mu\frac{\partial u_k}{\partial x_k}\delta_{ij} \tag{2.7}$$

$$q_i = -k\frac{\partial T}{\partial x_i} \tag{2.8}$$

Where p is the pressure, μ is the viscosity and k is the thermal conductivity. The transport coefficients were evaluated using the correlations given by White [42]. The working fluid (air) was assumed to be a calorically and thermally perfect gas such that $\epsilon = c_v T$ and $p = \rho RT$, where T is the temperature, c_v is the specific heat and R is the gas ideal constant. The spatial derivatives were evaluated with sixth-order compact differences, and stability was enforced with an eighth-order Padé-type filter. Near the domain boundaries, the filter order was reduced in steps of two, with no filtering at the boundary itself. Similarly, the accuracy of the spatial scheme was reduced to fifth-order and fourth-order accuracy near boundaries. Time marching was carried out using a second-order implicit scheme. Further details on the numerical methods of the solver are given in [41]. For validation of the numerical model the experimental results of Elena and Lacharme [43], Alving [44] and Konrad [45] for the streamwise velocity profile of a turbulent boundary layer and the Reynolds normal stress were used, as presented in [41] and [37].

Unsteady Reynolds-Averaged Navier-Stokes Simulations

To assess the capabilities of Reynolds-averaged Navier-Stokes solvers modelling the free-stream transient evolution impact on the near wall region the commercial software ANSYS Fluent ® was used. To reduce the computational burden the simulations on this solver were carried out on a 2D version, considering the center-plane of the domain. The plane was meshed following a blocking strategy with ANSYS ICEM ®. In order to guarantee a proper geometrical discretization, a grid sensitivity study was accomplished following the approach outlined by Celik et al. [46]. For this purpose, the axial flow velocity just outside of the boundary layer and the boundary layer momentum thickness were acquired for all the different grids. The different spatial discretization models were tested at the final steady state condition, P_0 = 20.5 kPa, T_0 = 500 K, T_{wall} = 300 K, P = 16 kPa. A summary of the different mesh properties is also presented in Table 2.

Table 2: Mesh sensitivity for 2D URANS simulations

Cell Count	N_x	N_y	u_∞(m/s)	θ (mm)	GCI %
48600	270	180	260.9	2.6	33.8
83200	320	260	261.6	2.4	10.8
140000	400	350	261.94	2.34	1.8
235200	560	420	261.98	2.33	1.7
400000	800	500	261.95	2.34	

The mesh with 140000 cells was selected for the transient evaluation given its accuracy compared to the finer cases and its grid convergence indicator. To enhance correct near wall flow prediction the y^+ was maintained below 0.5 along the entire plate. Due to the non-stationary flow behavior, and in order to resolve quantitatively the aerodynamic structures and the wall fluxes evolutions Unsteady Reynolds-averaged Navier-Stokes Simulations were evaluated. In this approach the turbulence closure was achieved through the use of the Langtry-Menter four-equation Transitional SST model [47]. The working fluid was air, modeled as an ideal gas. The Sutherland law was implemented to include the effect of the temperature on the molecular fluid viscosity. Second-order upwind schemes were adopted for the flow and turbulent kinetic energy, while second order implicit schemes were used for the transient formulation. This methodology was previously verified against experimental results on flat plate accelerated flow, presented in [48].

Table 3: DNS vs URANS for steady flow conditions

	Flow Conditions				
	P_0 (kPa)	T_0 (K)	T_w(K)	P (kPa)	θ (mm)
DNS	17	500	300	16	2.8
URANS	17	500	300	16	2.89
DNS	20.5	500	300	16	2.24
URANS	20.5	500	300	16	2.34

Figure 4 a) and b) compare the axial velocity and density boundary layer profiles for URANS and DNS simulations at the initial and final steady flow conditions of the evolution. The URANS results slightly depart from the DNS profiles near the wall region, which falls within the accuracy of the URANS models on predicting the near wall region under this low Reynolds number environment. In terms of the momentum boundary layer thicknesses the integral values obtained are displayed in Table 3; the URANS have only a 5% deviation from the DNS results. Figure 4 c) depicts the shear stress profiles at initial and final conditions for both solvers. For the initial steady flow condition URANS transitional model predicts an earlier fully developed turbulent boundary layer and the magnitude of shear stress along the plate does not deviate much

from the DNS. However, for the final flow condition at higher Reynolds number the URANS also predict an earlier complete transition but the axial shear stress magnitude deviates about 30% from the Direct Numerical Simulation results. In addition to the turbulent simulations laminar evaluations were carried out to compare the impact of sudden free-stream variations over laminar and turbulent boundary layers.

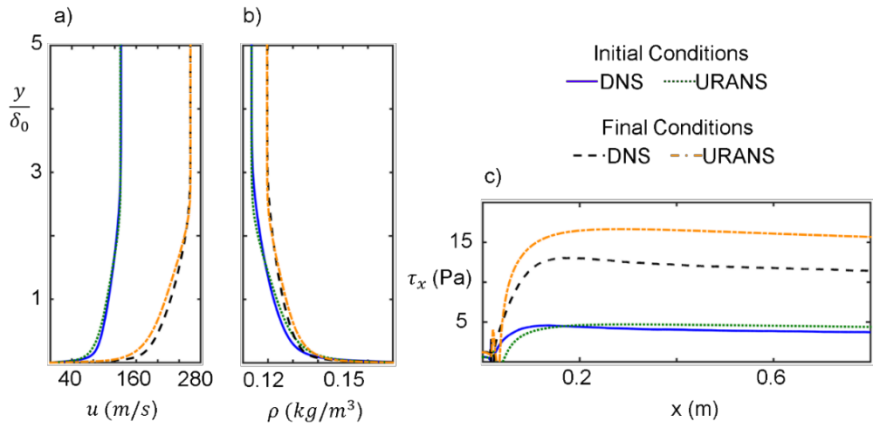

Figure 4: Steady State Comparison DNS vs URANS

Boundary layer and wall fluxes evolution after sudden flow acceleration

Figure 5 represents the evolution of the gas density across the center-plane of the domain for several time steps along the flow acceleration. The first image corresponds to the conditions prior to the total pressure rise. The boundary layer transition is enhanced by the tripping near the domain inlet and fully developed turbulent boundary layer flow is present in the second half of the domain. The second time step depicts the density contour at half of the total pressure rise. Due to the passage of the pressure waves slightly larger density is present near the plate leading edge. This phenomenon is further enhanced once the final total pressure is set at t=46.4 ms. As a consequence of the delay on the arrival of the expansion waves from the outlet, the density at the front of the domain is up to 15% larger than at the trailing edge of the plate. Finally, the domain establishes at the final condition as depicted for t = 99 ms.

Figure 6 a) depicts the axial free-stream velocity (u_∞) temporal evolution at y = $7\delta_0$ at the end of the resolved region, L^x. The results from DNS, URANS and the laminar simulation fall on top of each other, depicting the same acoustic response in the three numerical setups for the imposed transient. Similarly, Figure 6 b) displays the flow acceleration parameter, (k), at the same location. The acceleration parameter:

$$k = \frac{\mu}{\rho u_\infty^2}\frac{du_\infty}{dx} \tag{3.1}$$

represents the acceleration rate progress along the transient right at the end of the resolved region. This factor is commonly used for the prediction of flow relaminarisation [49, 50]. There are two different phases present in the acceleration. At first, following the arrival of the initial pressure wave the acceleration parameter displays negative magnitude. Figure 7 represents the propagation of the characteristics along the domain following the total pressure raise at the inlet. As the total pressure increases in the inlet to initiate the acceleration a pressure wave is released. The pressure wave travels along the domain at the speed of sound (c) plus the actual free-stream velocity (u). As the pressure wave cruises over the plate it accelerates the flow, and consequently faster flow is present behind it, driving a negative acceleration parameter. Once the pressure front reaches the domain outlet it is reflected as an expansion wave that travels upstream at c

– u. The arrival of the expansion wave at the observation plane is represented by the increment of the acceleration parameter. The peak of acceleration parameter takes place for the final phases of the acceleration after the final steady state total pressure is set at the inlet. Figure 6 c) shows the local free-stream flow temporal acceleration throughout the transient. The maximum local acceleration takes place at t = 44 ms, right at the inflexion point on the acceleration parameter, when compression and expansion waves meet at the edge of the finely resolved region.

The impact of the free-stream flow conditions is directly reflected in the near wall region as represented in Figure 8 a) and b) for the wall shear stress and heat flux respectively. Figure 8 a) depicts the evolution of the axial wall shear stress at the end of the finely resolved region. Both turbulent simulations display similar trends, although as already discussed in the comparison for steady conditions the kω-SST model over predicts the wall flux magnitude at this low Reynolds number. There are two different phases present on the evolution of the heat flux, at first once the flow starts to react to the acceleration at L^x , t > 37.8 ms, the wall shear stress rapidly increases as a consequence of the free-stream velocity change and the boundary layer height reduction. Then for t > 49 ms the slope of the shear stress growth starts to decay. Finally, the drag approaches its final steady state in a logarithmic way. Figure 9 a) depicts the evolution of the momentum boundary thickness throughout the transient. The boundary layer suffers an initial rapid shrinkage driven by the passage of the compression waves, leading towards a minimal thickness at t ≈ 48.5 ms. The shrinkage is a consequence of the flow inertia, as the flow accelerates it pushes the low momentum flow inside of the boundary layer against the wall, reducing the overall boundary layer height and boosting the skin friction. After the minimum thickness the boundary layer height gradually approaches its final status. The overall change on the axial shear stress increase rate is driven by the interaction of the boundary layer thickness and free-stream velocity temporal evolution.

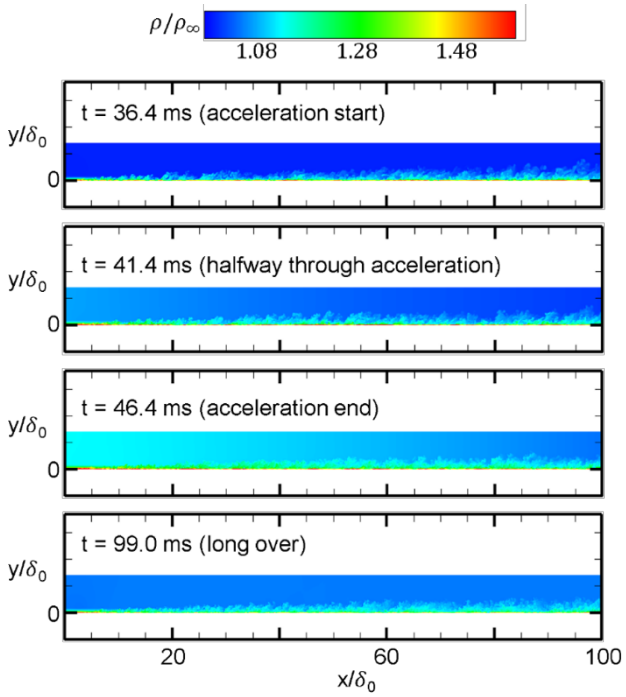

Figure 5: 2D contour of Density along center plane for several time steps along the transient evolution

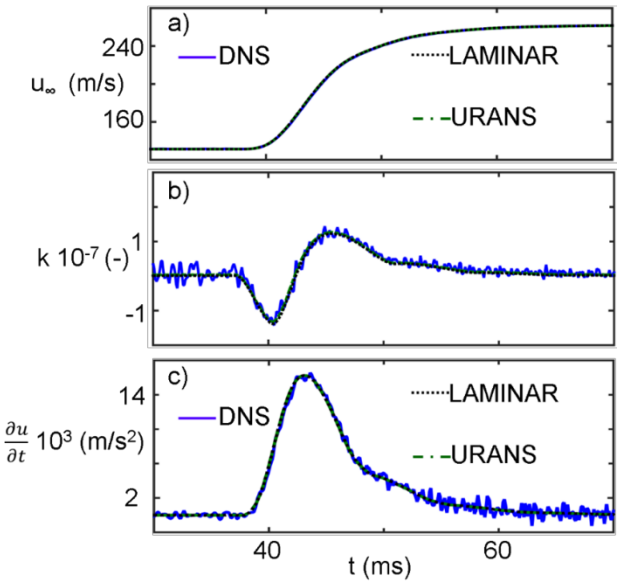

Figure 6: Temporal Evolution of Free-stream flow conditions through the transient for DNS, laminar and URANS simulation; a) Axial free-stream velocity, b) Flow acceleration parameter, c) Local flow acceleration

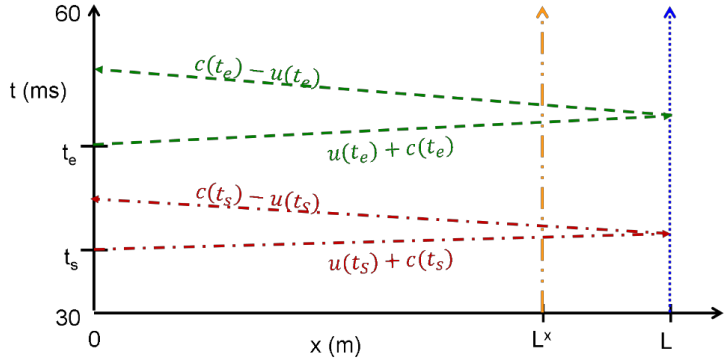

Figure 7: Acoustic propagation of total pressure waves generated at the inlet

In terms of the heat flux, as depicted in Figure 8 b) there is an intermediate phase on the temporal evolution driven by the reduction of the free-stream gas temperature. Throughout the simulation a constant total temperature is imposed at the inlet, consequently as the Mach number rises the static temperature of the flow is reduced. The change on the free stream temperature is convected downstream at the mean flow velocity and then diffused across the thermal boundary layer. For the laminar boundary layer temporal evolution there are also two clear trends after the acceleration outset. During the first segment of the local acceleration, t<44 ms, the wall fluxes magnitude increase following the reduction of the momentum boundary layer thickness and the increase on the local free-stream acceleration. While for t>44 ms the shear stress follows a gradual decay towards the final steady state condition. The laminar boundary layer actually overshoots the final value of wall fluxes during the transient driven by the sudden mean flow velocity change, depicting a stronger influence of the acceleration on the shear stress and heat flux. The laminar boundary layer also displays a slower adaptation or larger establishment delay to the final conditions as the propagation of the information across the near wall region is promoted only by the molecular diffusion.

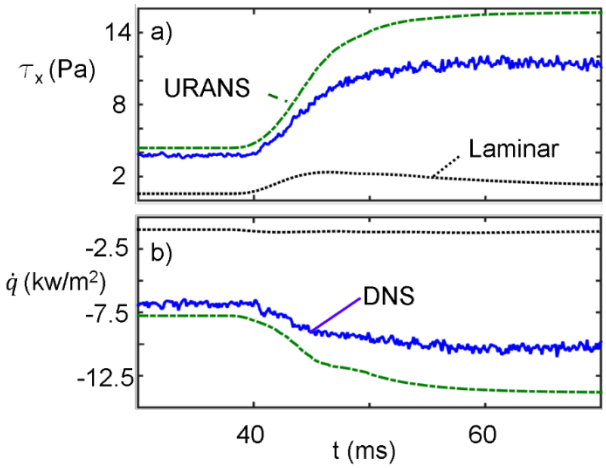

Figure 8: Impact of mean flow sudden acceleration on wall fluxes for DNS, laminar and URANS evaluations; a) Heat flux evolution, b) Stream-wise wall shear stress

Figure 9 b) represents the temporal evolution of the flow momentum contained inside of the boundary layer thickness. The definition used here for the boundary layer thickness is the height at which the local axial velocity is 99% of the free-stream one. Regardless of the boundary layer status, either turbulent or laminar, the flow momentum in the near wall region is boosted along the flow acceleration.

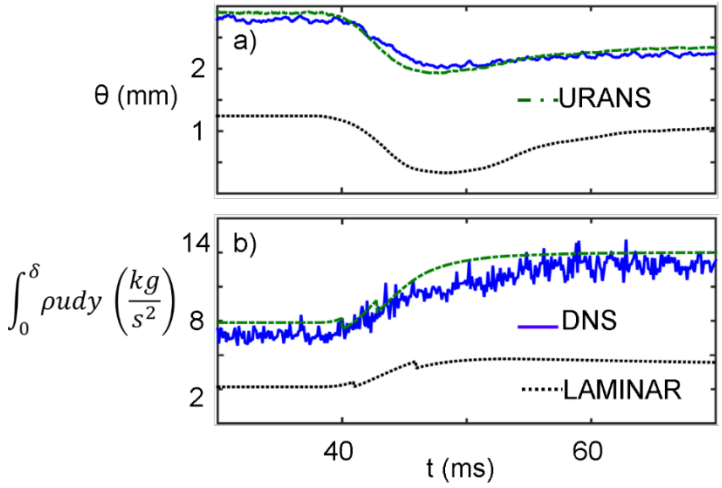

Figure 9: Near wall flow region temporal evolution through the flow acceleration for DNS, laminar and URANS simulations; a) Boundary layer momentum thickness, b) Integral flow momentum inside of the boundary layer along the transient

Figure 10 a) and b) represent the axial velocity profiles in inner and outer units for several time steps along the transient acceleration. All the profiles collapse in the viscous sublayer, depicting a negligible effect of the acceleration parameter on the inner boundary layer status during the phases of stronger acceleration. On the other hand, inside of the logarithmic region the profiles depart from each other, indicating that the distribution of hairpin-type vortices might be affected by the flow acceleration, and probably preventing the application of a universal von Karman constant under these circumstances, [51, 52]. In the outer stream wise velocity profiles all the time steps collapse for the near wall region $y/\delta_0 <$

0.2. However, the profiles at t = 0.0485 s and 0.053 s depict slightly higher velocities than the other profiles at $0.2 < y/\delta_0 < 2$ suffering the influence from the mean flow acceleration.

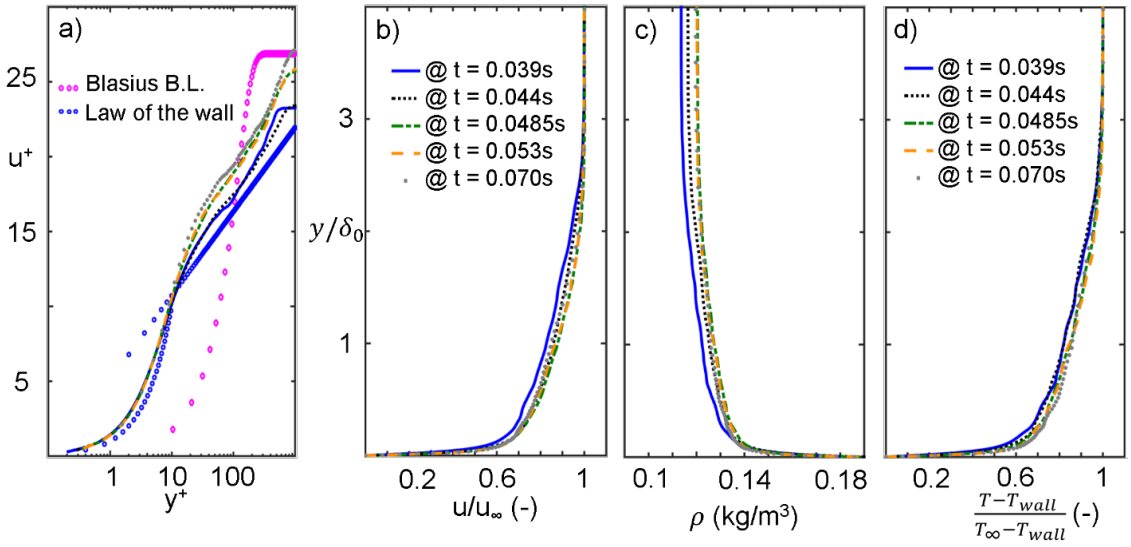

Figure 10: Boundary layer profiles during the sudden flow acceleration a) Inner unit axial velocity, b) Stream-wise velocity profile in outer units, c) Density d) non-dimensional temperature

Figure 10 c) and d) depict the profiles of density and referenced temperature along the wall normal direction at the end of the finely resolved region, $x = L^x$. The changes on the referenced temperature profiles are mainly driven by the evolution of the boundary layer thickness along the flow acceleration. The profiles at t = 0.0485 s and 0.053 s depict the smaller thermal boundary layer thickness of the transient, which is consistent with the evolution of the momentum boundary layer thickness considering the Reynolds analogy. However, in the density profiles representation further differences are observed when comparing different phases of the acceleration. The shifts on the density profiles are motivated by the travelling compression and expansion fronts carrying out the total pressure changes and its natural reflections at the domain outlet.

Figure 11 represents the normal velocity profiles obtained at L^x during several time steps along the acceleration. At stable free-stream conditions the integral normal flow velocity along the boundary layer has positive magnitude as a consequence of the axial growth of the displacement thickness. However, during the sudden flow acceleration for the profiles at maximum acceleration rate (t = 0.044 and t = 0.0485), the integral value of the normal velocity component is negative. Which remarks that the due to the passage of the compression wave passage the flow is being pushed towards the wall shrinking the boundary layer size.

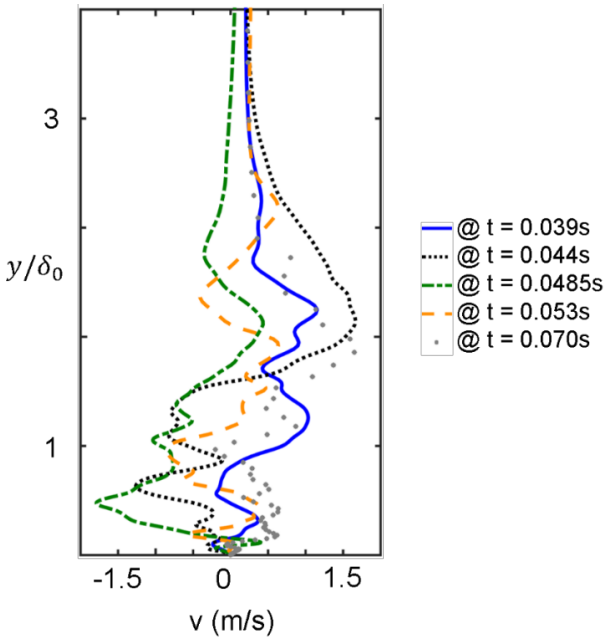

Figure 11: Wall normal velocity at different instances during the transient

Transient performance of separated flows

The aerothermal performance of the low pressure turbine in UAVs' is significantly abated at high altitude, due to boundary layer separation. During past years different flow control strategies have been proposed to prevent boundary layer separation, such as dielectric barrier discharges, synthetic jets, vortex generators. However, the optimization of the control approach requires a better characterization of the separated regions at several frequencies. The present chapter analyzes the behavior of separated flows, and specifically reports the characterization of the inception, reattachment and separation length, that allows the development of more efficient methods to enhance or abate flow separation under non-temporally uniform inlet conditions. The development of separated flows under sudden flow accelerations or pulsating inlet conditions were investigated with series of numerical simulations including Unsteady Reynolds Average Navier Stokes and Large Eddy Simulations. The present research was performed on a wall mounted hump which imposes an adverse pressure gradient representative of the suction side of low pressure turbines. The use of a smooth wall curvature geometry rather than a backward facing step unlocks the separation inception. The heat transfer and wall shear stresses were fully documented, as well as the flow velocity and temperature profiles at different axial locations to characterize the near wall flow properties and the thermal boundary layer. Through a sudden flow acceleration the dynamic response of the shear layer detachment as it is modulated by the mean flow evolution is investigated. Similarly, the behavior of the recirculation bubble under periodic disturbances imposed by sinusoidal inlet total pressure signals at various frequencies ranging from 10 to 500 Hz is studied. During each period the Reynolds number oscillates between 40000 and 180000 (based on a characteristic length of 0.1 m). Finally, as a first step into the flow control approach adding a slot in our geometry to allow flow injection and ingestion just upstream of the separation inception. Exploring the behavior of the separated region at different slot pressure conditions the envelope for its periodic actuation was defined. Thanks to that analysis, it was found that matching the actuator frequency with the frequency response of the separated region the performance of the actuation is boosted. The uprising use of UAVs and the breakthrough of the distributed thrust is promoting the design of ultra-compact and versatile gas turbine engines[53, 54]. The cruise operation of such power plants at high altitudes is narrowed because of the small Reynolds number through the low pressure turbine stages. At reduced Reynolds numbers <100000 (based on blade axial cord) the rear part of the blade suction can suffer flow separation, which dramatically lowers the stage efficiency [55]. Due to the flow separation, the flow capacity of the low pressure turbine stage is significantly reduced while the viscous loses are boosted [56]. This burdensome performance prevents its operation at higher altitudes and reduces the overall airframe range.

Many studies have been performed on the control of flow separation through passive and active techniques on the quest towards compact LPT stages integrations [57]. Gurney flaps concepts were proposed by Byerley et al. [58] to control the laminar flow separation on turbine blades. The flaps mounted on the pressure surface near the trailing edge, turn and accelerate the flow through the passage directing it towards the suction side. Preventing the flow separation, by reducing the adverse pressure gradient at low Reynolds conditions. Lake et al. [59] introduced the use of surface dimples to reduce the size of the separated flow regions. While, Volino [60] studied the effect of rectangular bars on the suction side surface to promote the boundary layer transition and encourage the flow reattachment. However, the passive flow control devices alter the performance of the vanes at higher Reynolds numbers, reducing the overall stage efficiency at lower altitudes. Consequently, low Reynolds tailored vane designs might be non-suitable for takeoff, climbing or landing environments. Which leads towards the integration of active flow control approaches to mitigate the flow separation when needed. Greenblatt and Wygnanski [61] documented the control of flow separation by periodic excitation through hydrodynamic excitation methods. Ranging from acoustic wave based approaches to flow suction or ingestion. The application of glow discharge plasma actuation on the boundary layer control has been experimentally [62] and numerically [63] proven. Determining its effectiveness promoting the transition in the shear layer, enhancing a fast flow reattachment.

On the other hand, single dielectric barrier discharge plasma actuators, (DBD), have been widely used for the suppression of the flow separation [64] [65]. Huang et al. [66], used DBDs on a low Reynolds number environment in a linear cascade. Similarly, Göksel et al. [67] looked into the efficiency impact of pulsed plasma actuators at various Reynolds numbers. The lower the Reynolds number, the most effective the control because of the increasing momentum coefficient. Porter et al. [68] detailed the effectiveness of the DBD plasma actuators tripping the boundary layer transition, which could alleviate and avoid the flow separation regardless of the actuator orientation. Based on surface pressure measurements, Post and Corke [69] analyzed the influence of plasma induced streamwise vortices and 2D axial jets on the airfoil suction surface at stall conditions. The plasma actuation enhanced the flow reattachment, boosting the lift to drag ratio at points beyond airfoil stall. In a similar way, Gaitonde et al. [70], applied asymmetric dielectric-barrier-discharge on stalled NACA symmetric airfoils. Evidencing the effectiveness of the streamlined actuation on the generation of wall jets that avoid the flow separation. Dielectric barrier discharges were also used by Rethmel et al. [71]. Generating coherent spanwise vortices that relocate momentum from the free stream into the near wall region, energizing the per se low momentum flow and endorsing the flow reattachment.

Many others authors propose the use of pulsed jets for the control of flow-separated regions based on the injection of flow from a higher pressure environment. Volino [72] used oscillating jet vortex generators to control the flow separation in the rear suction side of a low pressure turbine blade. The jets were injected into the suction side through spanwise orifices. Its effectiveness was demonstrated at a variety of frequencies and amplitudes. Similarly, Bons et al. [53] and Sondegaard et al [73], assessed the efficient control of laminar flow separation based on pulsed jets. Where the maximum effective frequencies were limited by the settlement time of the boundary layer as it reattaches. The presence of unsteady flow conditions on the low pressure turbine will affect the behavior of the flow separated regions and its reaction to any flow control approach. In this regard, Schobeiri et al. [74] provided experimental data describing the evolution of inception and separated flow region as a consequence of unsteady mean flow conditions. Where the wake passing had a strong influence on the recirculation bubble, modulating its extension. In a similar way, Wissink [75], numerically investigated the effect of incoming wakes on a low pressure turbine cascade with DNS simulations. Where also the influence of the incoming flow disturbances on the separated flow region was highlighted.

In this section, a research on the dynamic response of flow separated regions and its control based on a wall mounted hump domain is presented. The use of a smooth wall curvature geometry unlocks the separation inception, which then becomes on a relevant variable to determine the most effective near wall flow control. Wall mounted humps have been previously used under such circumstances on wind tunnel experiments at high Reynolds numbers [76]. Similarly, turbulent flow separation control experiments over wall mounted humps using dielectric barrier discharge have been documented [77-79]. In fact, He et al. [77] compared the experimental results with URANS analysis validating the use of several turbulent models resolving such flow structures. Through URANS and LES simulations, the dynamic response of the flow separated regions to mean flow periodic excitations or sudden flow accelerations were studied. Which reveal the strong dependence of the recirculation bubble on the mean flow velocity variations.

Many flow operated devices are exposed to flow separation and reattachment in a variety of a geometrical locations. The flow separation may be induced by rear flow facing steps[80, 81], positive pressure gradients [82-84], shock boundary layer interaction[85-87] or induced by unsteady flow impingement [74, 75, 88]. Particularly, many industrial heat exchangers exploit the mixing induced in the separated shear layer to magnify the heat transfer rate. In quest towards the performance improvement on the heat exchangers operation as well as aerodynamically driven process a proper understanding of the flow separation is required. Many authors have proposed different techniques on the flow separation control with two coupled objectives: heat transfer enhancement and minimization of aerodynamic loses. [61, 76, 89-91] [92]. However, it is generally found that the flow control approaches rely on passive devices, random

periodic excitations or pulsating frequencies only found after optimization analysis. Following this principles the energy required to perform the flow control may exceed the actual requirement for effective flow control. Aiming a performance increase not only in terms of heat transfer enhancement or aerodynamic footprint, but also on an efficient and effective flow control the dynamic scales of flow separation are investigated.

The flow over a backward facing step has been extensively documented in both empirical and numerical studies.[93] [94] [95]. The investigation of the turbulent shear layer over a back-ward facing step has been conducive to the reattached boundary layer flow characteristics as well as the features flow reattachment [96]. The flow features for different expansion ratios were disclosed by Biswas et al [97], where a strong wo-dimensional behavior was recognized. Similarly the analyses of several Reynolds number was conducive to the understanding of the different separated region geometrical scales. The research on the unsteadiness and the convective instabilities over the backward-facing step conducted by Kaiktsis et al. [98] revealed the characteristics of the disturbances propagation. It was found that the small disturbances were transmitted downstream with significant amplification with a local convective speed. Additional excitations into the shear layer region were only found to be altering the flow separation characteristics only at high frequency rates. Which is a symptom of the magnitude of the dynamic scales which control the shear layer region. Similarly, based on LES simulations the effects of periodic perturbations inside of the detached shear layer behind a rear facing step have been qualified. Where again, the Strouhal number has been proven to notoriously affect the interaction between the shear layers instabilities.[95] Based on DNS simulations, Kaiktsis et al [98] indicated that the 3 dimensionality onset takes place in the thresholds between primary and secondary recirculated regions. Which emphasizes the presence of secondary instabilities in the shear layers being triggered by the corner vortex. Combined heat transfer and aerodynamic measurements performed by Vogel and Eaton [99] explained the heat flux distribution downstream of a backward-facing step and its coupled nature with the fluid dynamic structures. Where fluctuating momentum and thermal boundary layer profiles had a strong influence on the transient evolution of the heat transfer rate along the reattachment region. Hence, the efficient enhancement of the heat transfer rates could only be guaranteed by a deep understanding of the aerodynamic scales.

Methods assumptions and procedures

The experiments were carried out on the Purdue Experimental Turbine Aero-thermal Laboratory blow down linear wind tunnel [100]. The linear wind tunnel layout is presented in Figure 12 a), 56 cubic meters of dry compressed air are stored at 150 bar. Two different lines divert from the air storage, the first one is directly delivered to the test cell and discharges the flow in the mixer. The second line goes through a heat exchanger driven by a gas natural burner that provides non-vitiated air at higher flow temperatures. The heated supply is then combined with the cold stream in the mixer. The mass flow ratio between cold and hot flow settles the actual flow temperature. The mixed stream is then delivered to the facility through a calibrated critical venture that provides high accuracy mass flow measurements.

During start-up procedures and while achieving uniform flow conditions, the air is vented through a purge line. Once the facility operates at steady conditions, the butterfly valve upstream of the linear wind tunnel settling chamber is open and the purge valve is closed. Finally, the flow is discharged in the vacuum tank through a sonic valve. The use of the sonic valve allows the settlement of the downstream static pressure independently of the vacuum tank conditions. Taking advantage of the sonic valve and varying the mass flow ratio between the cold and hot line, Reynolds and Mach number are independently adjusted.

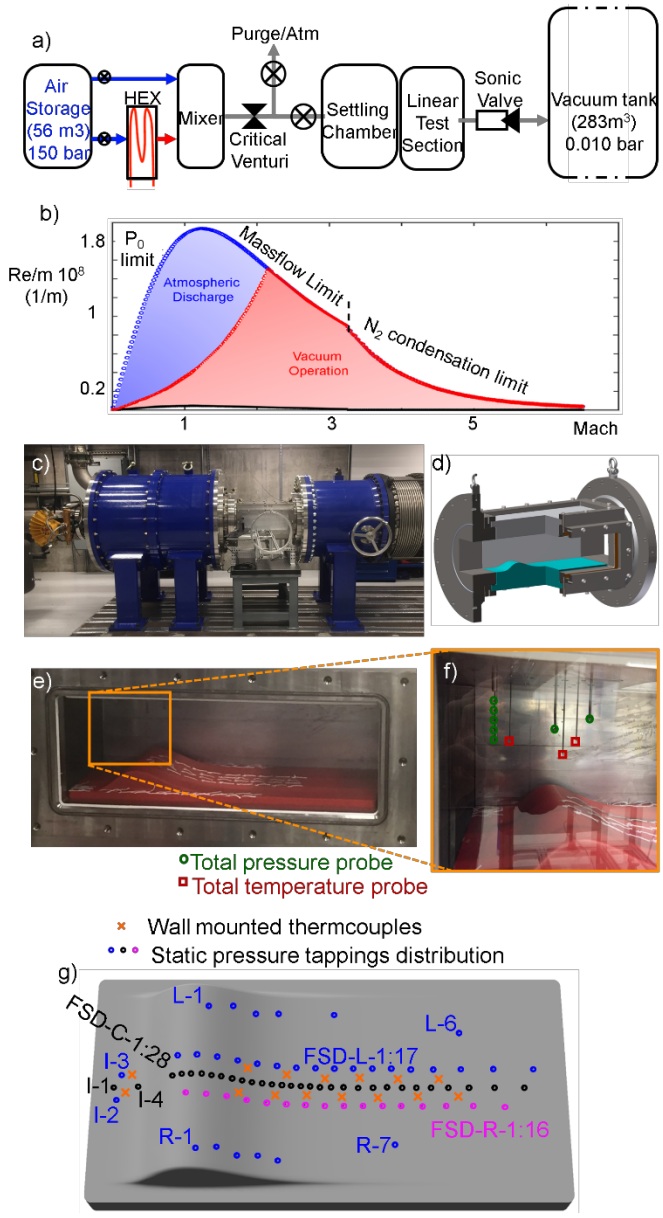

Figure 12: Experimental apparatus: a) Facility layout, b) test section, c) flow separation domain integration in the linear test section, d) e) test section, f) Wall mounted thermocouples and surface taps distributed along the test article

The operational envelope of the linear wind tunnel is presented in Figure 12 b). During subsonic operation, the upper limit in Reynolds is constrained by the maximum operational pressure and the maximum massflow that can be flowed through the upstream piping. To explore lower Reynolds the wind tunnel is connected to the vacuum tank and the downstream pressure is lowered until 0.01 bar. The linear test section can operate in supersonic and hypersonic conditions by introducing a convergent-divergent nozzle following the area contraction of the flow conditioning system. At hypersonic flow conditions, the upper limit of the Reynolds number is constrained by the condensation of Nitrogen. Figure 12 c) depicts the Purdue Experimental Turbine Aerothermal Laboratory linear test section. Figure 12 d) represents the sketch of the 3D flow separation domain integrated in the linear wind tunnel. To minimize the light and laser reflection from the test article the aluminum surface was coated with Cerakote red ceramic paint.

Figure 12 e) shows the coated test article installed in the test section. For simple flow visualization cotton tufts were installed over the hump rise, fall and side slots during some experiments. Figure 12 f) depicts the location of the total pressure and temperature probes. A total pressure rake with 5 heads and two total pressure Kiel probes were used to monitor free stream evolution during the experimental campaign. The total pressure readings were monitored with a Scanivalve MPS pressure scanner at a sampling frequency of 850 Hz. 1/16th tubing connections with a length of 0.15 m were used to guide the pressure signal to the transducers. The length and size of the tubing connections were selected to enhance the highest pressure frequency resolution. Several exposed k-type thermocouples were distributed along the test section centerline to identify the total temperature evolution.

Figure 12 g) represents the location of the pressure taps and wall temperature thermocouples along the test article surface. In total, 15 wall mounted thermocouples were distributed across the flow separation domain. On the other hand, 5 thermocouples were mounted on the back of the test article to monitor its temperature evolution and provide the back reference temperature for heat flux computation. The sensing element was glued with Kapton tape to the surface. The entire unsteady surface-temperature data acquisition was done at a sampling frequency of 1 kHz. A total of 78 pressure taps were perforated along the test article to monitor the evolution of the wall pressure during the experiments. The surface taps were distributed in 4 different regions. A cluster of 4 points identified by the indicator I-# was installed near the centerline of the domain on the leading edge of the test article. 6 taps were installed near the left boundary identified with the indicator L-# while 7 taps were perforated near the right boundary of the hump, R-#. Finally, 61 surface taps were distributed in three different groups near the center of the domain. 28 pressure taps were dispersed from the hump summit up to the trailing edge of the domain at half span of the test article. The rest of the surface taps were collocated 5% of the span away from the center. Additionally, 10 wall pressure readings were installed on the upper side of the domain scattered among the instrumentation inserts to monitor the evolution of the static pressure on the opposite surface. The wall pressure was recorded with a Scanivalve MPS unit with a 15-psi range. The surface taps were connected to the pressure scanner through 0.1 m long and 1/16" diameter nylon tubing. The pressure taps were scanned with a sampling frequency of 850 Hz. However, during the transient performance experiments, only the centerline pressure taps were monitored to boost the sampling frequency up to 2.5 kHz.

In addition to the pressure and temperature measurements, the stream-wise velocity component were also monitored with a mono-dimensional hotwire, with a wire diameter of 6.3 μm. The experimental assessment of the flow separation performance under mean flow unsteadiness is divided in two phases. During the first part of the campaign, only steady conditions were acquired. Aiming the characterization of the domain at different flow conditions. The second phase of the experimental campaign was focused on the effect of mean flow transients on the performance of separated flow regions. The mean flow variations were imposed by the fast acting valve located upstream of the settling chamber. The actuator of the valve was boosted to guarantee the fast aperture and closure of the valve (approximately 50 ms), allowing the sudden flow discharge into the settling chamber.

Steady state performance of flow separation domain

Figure 13 a) represents the static pressure distribution along the Flow Separation Domain for multiple Reynolds/m, ranging from 1.1×10^6 up to 5.2×10^6. Table 4 presents a summary of the mean flow experimental conditions: dynamic pressure at the test section inlet, total temperature, Mach number, and mass-flow through the test section. The flow downstream of the test section was directly discharged to atmospheric conditions.

Figure 13 b) depicts the reattachment location over the range of explored Reynolds numbers. The reattachment location was identified by the end of the plateau on the wall pressure distribution. The uncertainty associated to its measurement is the maximum distance to the nearest surface tap either in the

upstream or downstream direction. Figure 14 a) represents the pressure coefficient (c_p) distribution along the test article when operating at attached flow conditions, Re\m $7.4x10^6$. 3D URANS numerical results are compared against the experimental profile. Where the reference pressure, P_{ref}, is the outlet static pressure. In case of attached flow conditions there is an excellent agreement between the numerical and experimental results. Figure **14** b) depicts the pressure coefficient variation along the hump. The shape of the domain imposes an expansion, reaching a maximum gradient of 65 % at the pinnacle of the domain while the largest diffusion during the hump fall is near 40 %.

Table 4: Experimental matrix

Re/m (1/m)	Inlet Dynamic. Pressure (Pa)	$T_{0\,(K)}$	Mach	Massflow (kg/s)
1.1×10^6	140.8	290	0.045	0.75
1.5×10^6	250	290	0.059	1.00
1.9×10^6	390	290	0.074	1.25
2.2×10^6	560	290	0.089	1.50
2.6×10^6	765	290	0.104	1.75
3.0×10^6	1000	290	0.119	2.00
3.7×10^6	1570	290	0.148	2.50
4.5×10^6	2260	290	0.178	3.00
5.2×10^6	3070	290	0.207	3.50
7.4×10^6	6000	290	0.289	4.90
9.4×10^5	465	290	0.081	1.00
1.7×10^6	1420	290	0.141	1.75

Figure 15 a) represents the static pressure contour over the test article at Re/m $2.2x10^6$. As the flow accelerates through the hump rise, the static pressure decays reaching its minimum over the hump summit. The recirculated flow region extends across 50% of the span of the test section displaying a constant level of static pressure. Then its size is gradually strained towards the center as the flow from the sides is entrained by the pressure gradient. The flow separation process follows the expected 2D flow separation behavior. However, the flow reattachment process is driven by 3D flow features, including the absorption of the flow near the lateral walls and the lift-up of the recirculated flow. Figure 15 b) represents the static pressure distribution along the wall-mounted hump at three different span locations, 45%. 50% and 55%. The agreement among the three span locations depicts the uniformity of the test article performance across its center.

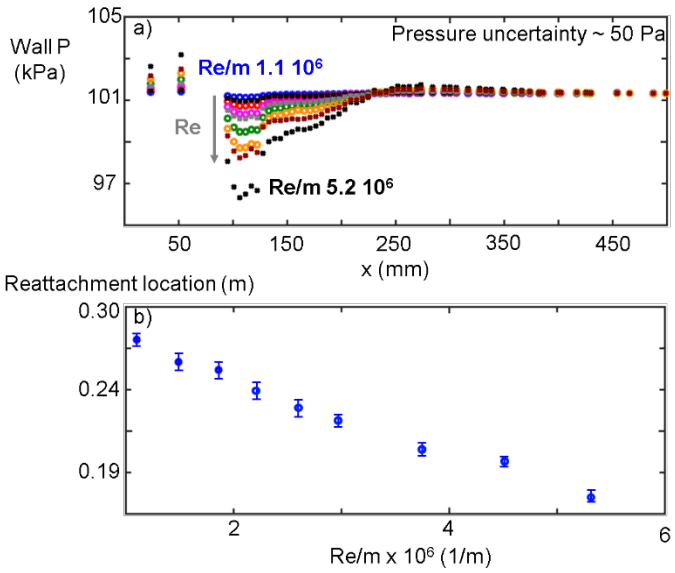

Figure 13: Flow Separation Domain performance at various Re/m

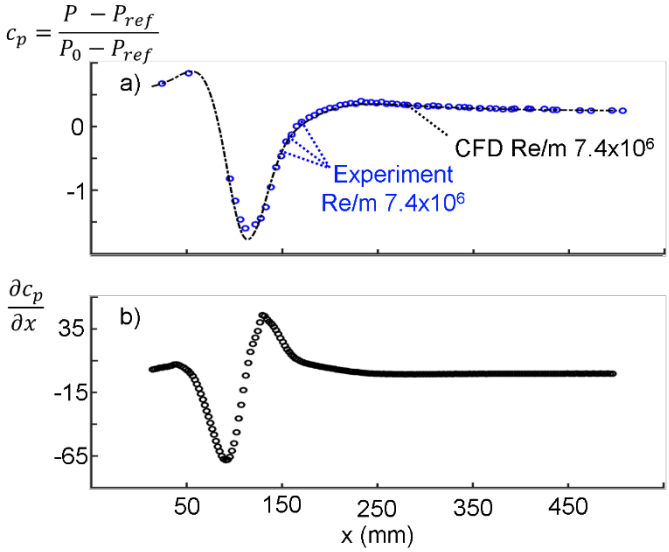

Figure 14: Test article performance at high Reynolds environments

Figure 16 and Figure 17 represent the hotwire traverses for conditions $1.5x10^6$ and $2.6x10^6$ respectively. Figure 16 a) depicts the stream-wise velocity profile at mid-span 210 mm downstream of the test article leading edge. The experimental results are compared against 3D-URANS simulations at the same axial location. Figure 16 b) represents the turbulence intensity at each one of the interrogated heights compared to the Turbulent Kinetic Energy numerical profile. The CFD prediction matches within the experimental uncertainty the velocity profile across the upper segment of the test section. Although, there is a mismatch on the axial velocity profile near the recirculated flow region prediction. The mono-dimensional hotwire sensor traversed across the test section height cannot accurately determine the flow velocity along the recirculated flow region. On the other hand, the turbulence intensity profile can also be a good indicator for the flow behavior under detached flow conditions. In this sense, based on the turbulence intensity profile when compared to the turbulent kinetic energy distribution, the current computational methodology can

predict the experimental trend. However, the predicted extension of separated flow region is larger than the experimental one. The peak of maximum turbulence intensity identifies the trace of the detached shear layer and its convection downstream.

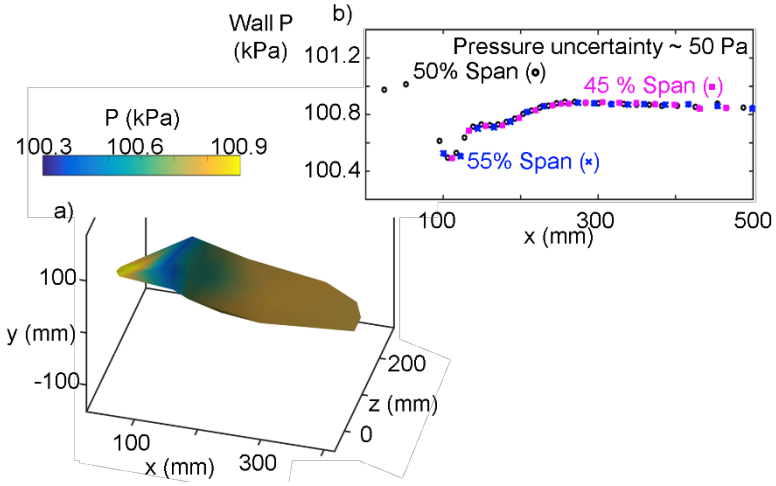

Figure 15: 3D Flow behavior at Re/m 2.6x10^6, a) Static pressure contour, b) Static pressure distribution along the test article center at various span locations

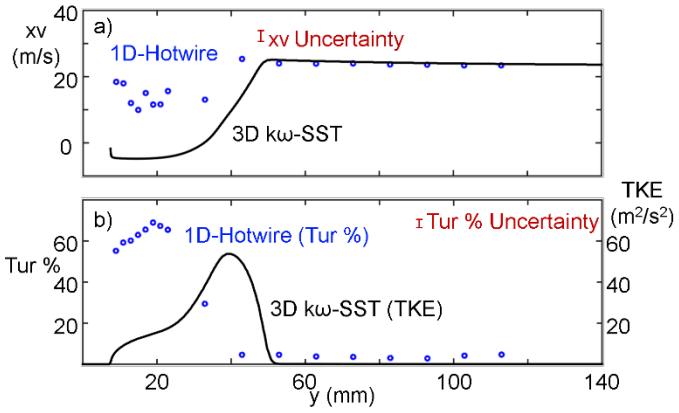

Figure 16: Hotwire Traverse at Re/m 1.5x10^6

Similarly, Figure 17 compares the hotwire axial velocity measurement and turbulence intensity to the numerical prediction based on the kω transitional SST turbulence model. As described for the operation at 1.5x10^6 conditions, the agreement between experimental and numerical results in the free stream flow is excellent. However, based on the extension of the recirculated flow region, the numerical model predicts a higher distortion on the axial velocity distribution due to the boundary layer separation. Although there is a mismatch on the actual extension of the recirculated flow region, the trend predicted by the numerical approach matches the experimental turbulence intensity distribution.

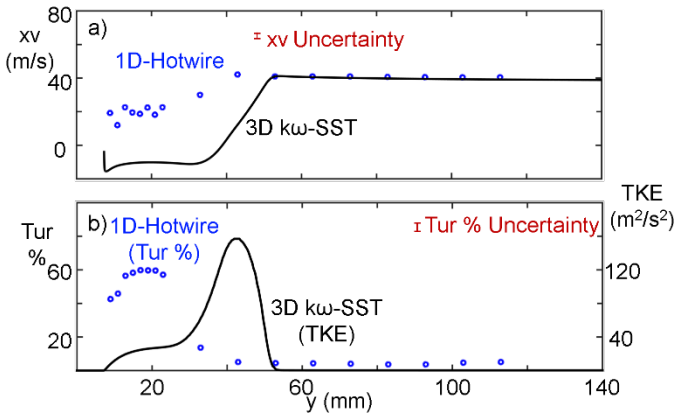

Figure 17: Hotwire Traverse at Re/m 2.6x10^6

Figure 18 represents the static pressure along the wall-mounted hump operating at Re/m 1.5 x 10^6. The experimental results are compared against 2D and 3D Unsteady Reynolds Averaged Navier Stokes Simulations with the kω SST Transitional turbulent model. Both 2D and 3D URANS cases are able to capture correctly the detachment inception of the boundary layer over the diffusion section of the hump. The origin on the pressure plateau on both CFD predictions matches the experimental results. However, both numerical models over-predict the extension of the recirculated flow region. In this line, the 3D case predicts an earlier reattachment compared to the 2D evaluation thanks to the influence of the 3D flow features, such as the lateral flow entrainment.

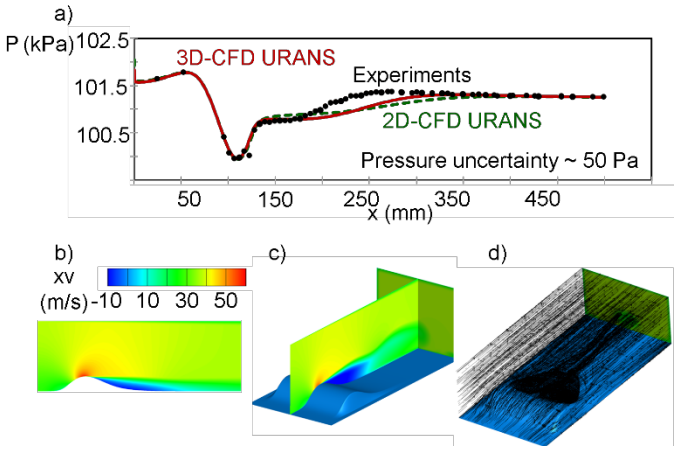

Figure 18: Unsteady Reynolds Average Navier Stokes prediction of separated flow regions compared against experimental results operating at Re/m 1.5x10^6

Experiments with larger temperature gradients between mean flow and test article (Re/m 9.4x10^5 and 1.7x10^6) were performed to compare the prediction of heat transfer distribution along separated flow regions with the current numerical methodology. Figure 19 represents the temporal evolution of the total pressure, total temperature and free stream axial velocity during the heat transfer experiments. There are peaks on the total pressure and axial flow velocity driven by the flow aspiration while purge and linear butterfly valves are simultaneously open during the start-up and shutdown of the experiment. However, during the core of the experiment the total pressure and axial free stream velocity depict steady mean flow operation. On the other hand, caused by the wind tunnel hardware warm-up, the total temperature in the

test section is continuously rising. Only after 1 minute of operation the slope of the temperature seems to decay and more stable conditions are achieved, at t = 60 s for $9.4x10^5$ and at t = 85 s for $1.7x10^6$. Figure 20 a) and b) represent the temporal evolution of three wall-mounted thermocouples over the hump surface for $9.4x10^5$ and $1.7x10^6$ operation respectively. The thermocouple at x=70 mm displays the larger temperature rise driven by the smaller boundary layer thickness at its axial location, while the ones at x=190mm and x = 370 mm are within the recirculated flow region and downstream of the reattachment point respectively.

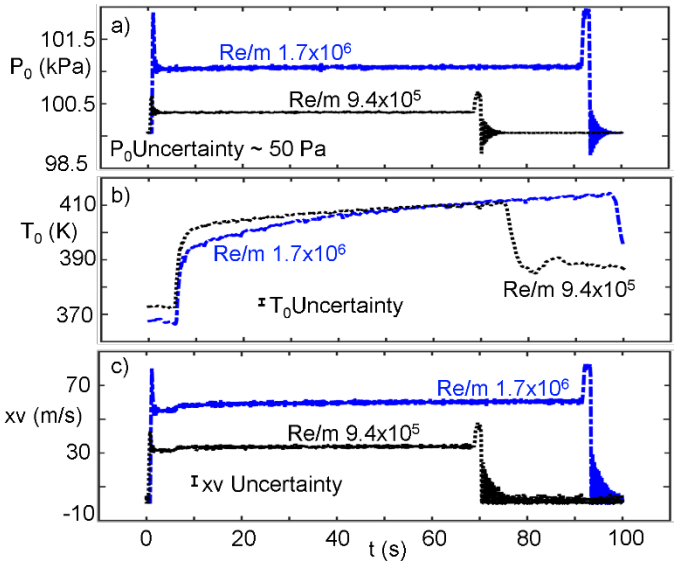

Figure 19: Hot flow experiments mean flow conditions

Taking advantage of the transient evolution of the wall temperature readings at the hump surface, the heat transfer coefficient is derived following the approached outlined by Saavedra et al. in [101]. Assuming 1-D heat flux conduction the heat flux is computed from the wall temperature readings on both sides of the test article. Then based on the flow total pressure and temperature temporal evolution together with the slope of the heat flux with respect to the wall temperature progression, the adiabatic wall temperature is retrieved. Afterwards, the heat transfer coefficient is computed from the ratio between the heat flux and the difference between the adiabatic and the actual wall temperature.

Figure 21 represents the heat transfer coefficient along the test article centerline for both operational conditions and its comparison against 3D Unsteady Reynolds Average Navier Stokes results (kω transitional SST). Throughout the initial attached flow region the CFD simulations predicted similar heat transfer levels and the results follow the trend marked by the experiments. The numerical evaluations were performed assuming the development of the boundary layer from the leading edge of the domain and with an inlet turbulence level of 3.8 %, matching the wind tunnel turbulence level of the facility. The predicted heat transfer coefficient throughout the hump fall also under-estimates the experimental heat transfer coefficient. Where again the over-prediction of the recirculated flow region extension is reflected on the axial distance difference between the peaks of maximum heat transfer downstream of the hump summit. Closely upstream of the reattachment location the heat transfer is maximum due to the reattached flow impingement, [99]. The experimental trend at Re/m $9.4x10^5$ shows a reattachment location $x \subseteq [210 - 235]$ mm while the numerical simulation predicts the reattachment around x=245 mm. Similarly, for operation

at Re/m 1.7x10^6 the reattachment happens nearby x = 200 mm or even further upstream, while the URANS reattachment prediction is at x = 230 mm.

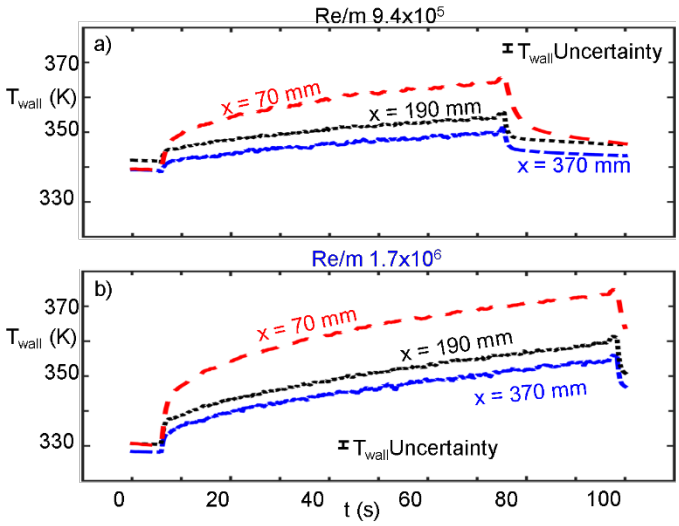

Figure 20: Wall temperature evolution at different axial locations along the hump surface for hot flow conditions

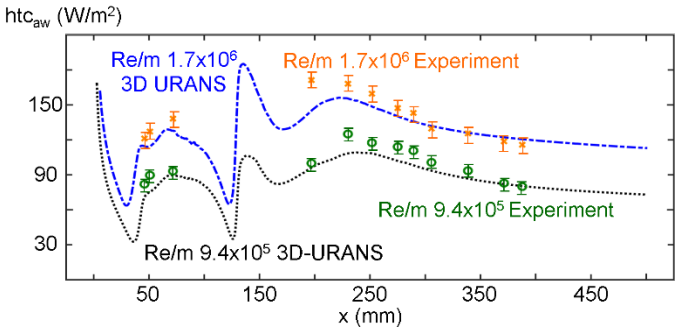

Figure 21: Heat transfer coefficient distribution along the hump surface operating at two different Reynolds numbers, comparison between experimental and numerical results

Flow separation performance under sudden flow discharge

After characterizing the performance of the test article under steady state operational conditions the impact of sudden mean flow changes on the boundary layer detachment is explored. Figure 22 represents the evolution of the mean flow properties during sudden flow discharge at Re/m 1.9x10^6 and 2.6x10^6 mean flow nominal conditions. The air stream was vented through the purge line during the start-up of the facility while the critical flow Venturi reached stable operation. Once the massflow was stable, the butterfly valve was actuated and the flow was discharged to the linear wind tunnel settling chamber. Figure 22 b) represents the total pressure evolution at the test section inlet for both experiments. Figure 22 c) depicts the transient evolution of the total flow temperature during the experiment. Which is characterized by the sudden temperature drop once the flow is released into the test section. Similarly, Figure 22 d) represents the stream-wise velocity evolution at the inlet of the test section. The represented velocity is derived from the local total pressure probe and static pressure readings in the upper wall of the test section at the inlet. The

purge line was re-opened and the butterfly linear test section was closed to set stagnant flow conditions before the sudden flow discharge at Re/m 2.6x10^6.

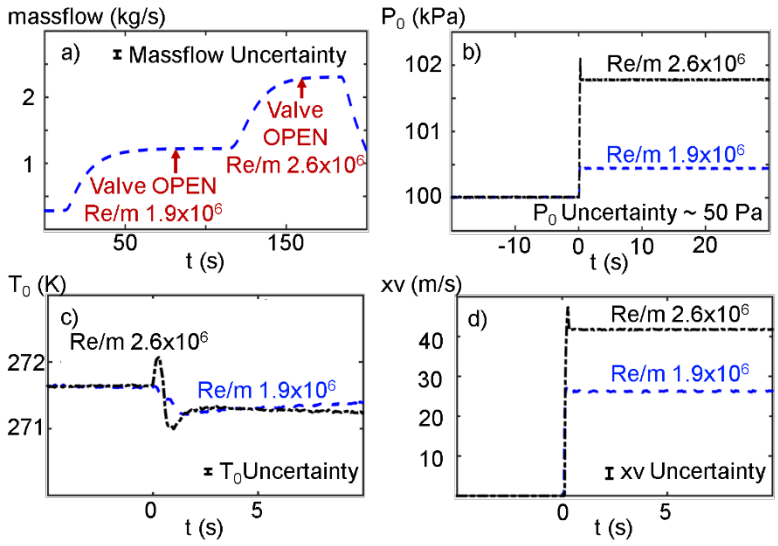

Figure 22: Sudden flow discharge experiment 1.9x10^6 and 2.6x10^6 conditions, massflow, total pressure, total temperature and axial free stream velocity

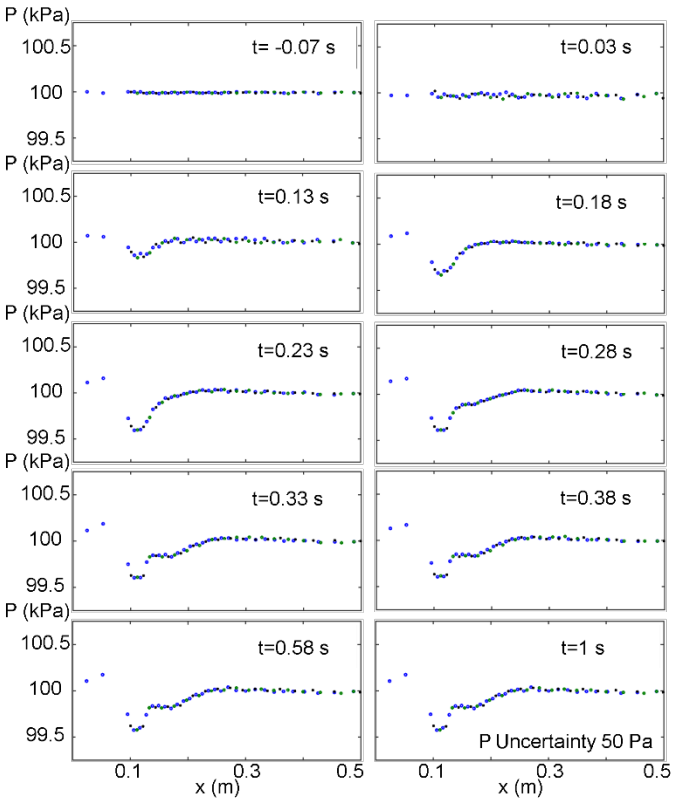

Figure 23: Surface pressure evolution during 1.9x10^6 sudden discharge experiment

Figure 23 illustrates the wall pressure distribution along the hump centerline for several time steps along the transient evolution. The pressure was monitored at 2.5 kHz and then a low pass filter at 400 Hz was applied to the transient signal at each axial location. Prior to the valve aperture, t = - 0.07 s, the entire test section has stagnant flow and the surface taps display the atmospheric pressure. Once the valve is open, the passage of the initial compression waves is felt as a local rise of the static pressure along the test article axis, t = 0.03 s. After the main pressure wave has travelled through the settling chamber and arrived to the test section, the flow is set into motion, t = 0.13 s. As the inlet flow velocity increases, the pressure distribution exerted by the hump geometry appears, reducing the static pressure towards the hump pinnacle followed by the diffusion along the fall. The dynamic pressure at the domain inlet gradually increases as the mean flow approaches the nominal flow velocity, driving stronger expansion and diffusion across, t = 0.18 s and t = 0.23 s. For later time steps, t= 0.28 s the mean flow conditions have already achieved their nominal values and a pressure plateau appears through the diffusion segment of the hump. Which illustrates the boundary layer detachment and the generation of the recirculated flow region. Following the boundary layer initial detachment, the recirculated flow region grows, t = 0.33 s, until it achieves its final extension, t > 0.38 s. During the first instances of the sudden flow release although the hump is already imposing the diffusion through its descent, the boundary layer does not detach.

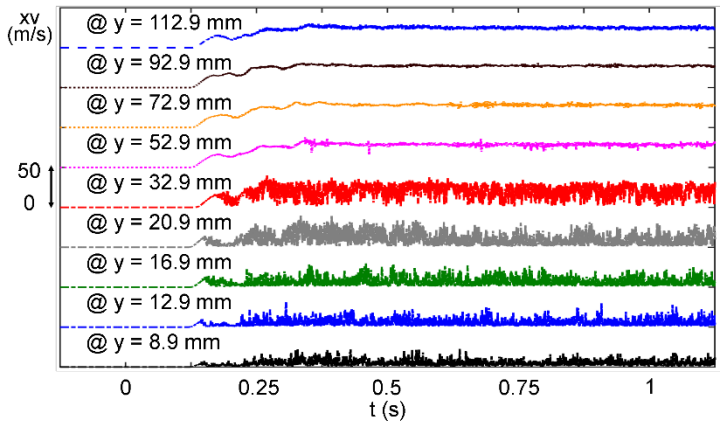

Figure 24: Stream-wise velocity transient evolution during Re/m 1.9x10^6 sudden

The near wall region receives a momentum boost in terms of boundary layer height reduction driven by the flow inertia,[102]. Under such circumstances, the boundary layer is able to overcome the adverse pressure gradient. Once the acceleration rate of the flow decays and the momentum boost vanishes, the boundary layer detaches from the wall and the recirculated flow region is generated. Figure 24 represents the temporal evolution of the stream-wise velocity component at various normal distances from the wall, 190 mm downstream of the test article inlet and 60 mm downstream of the hump summit. The profiles above the recirculated flow region, (y=72.9, 92.9 and 112.9 mm) follow the same trend, depicting the evolution of the mean flow velocity during the sudden discharge experiment. Following the arrival of the initial compression wave the flow velocity suddenly increases. Then it reaches a uniform value at t = 0.140 s to suffer a second increase towards the final flow velocity. The flow acceleration trend is promoted by the passage of the latest compression wave and the arrival of the expansion waves from the test section outlet. The measurements were obtained with a mono-dimensional hotwire probe. Hence the magnitude of the axial velocity component within the recirculated flow region (y<35 mm) does not reflect only the stream-wise velocity but also the influence of the transversal components. However, relevant information can be extracted from the transient trends about the development of the recirculated flow region by looking at the local flow unsteadiness.

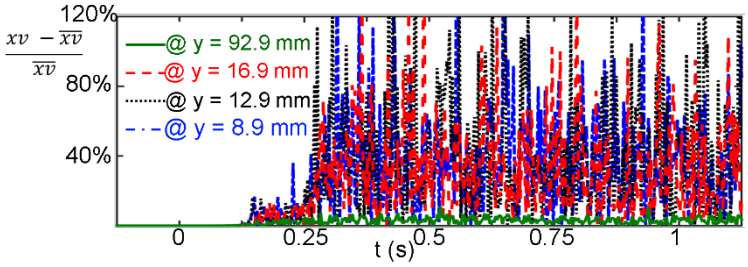

Figure 25: Local axial velocity unsteadiness during Re/m 1.9x10^6 Sudden

Figure 25 represents the stream-wise velocity component deviation from the average local velocity. The averaged local velocity is obtained applying a low pass filter at 20 Hz to the transient signal. This indicator is a measure of the temporal evolution of the local unsteadiness or flow turbulence at each normal location. For mean flow conditions, 92.9 mm, the local stream-wise unsteadiness remains within the wind tunnel inlet turbulence level, 4 %. However, this indicator displays larger magnitudes for the profiles nearer to the wall due to the flow recirculation. Interestingly, during the initial phases of the sudden flow discharge the local unsteadiness is one order of magnitude smaller than for the nominal flow operation, which is in agreement with wall pressure distribution transient evolution. Revealing the abatement of the boundary layer detachment during the transient acceleration phase.

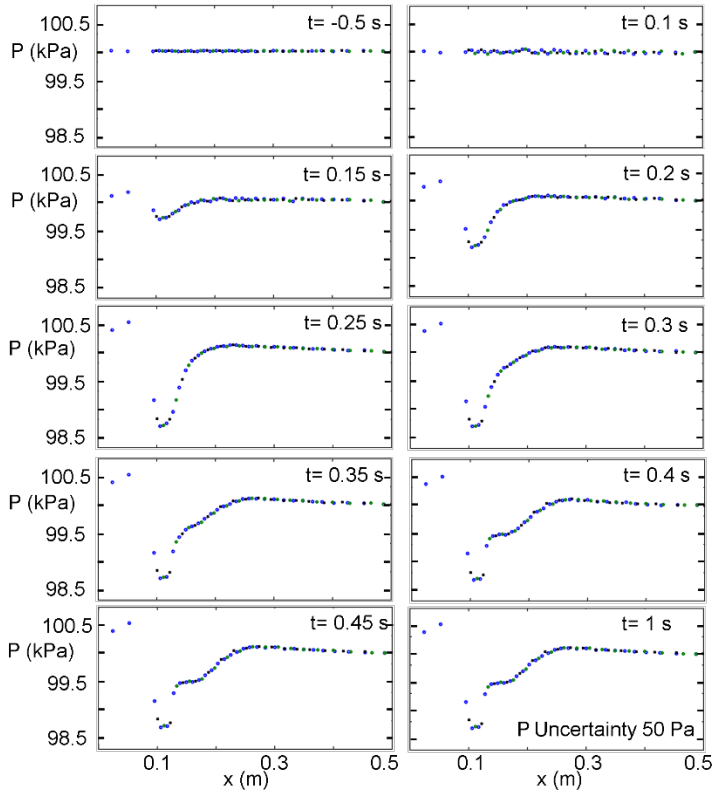

Figure 26: Surface pressure evolution during 2.6x10^6 sudden discharge experiment

In order to explore the impact of larger magnitude accelerations, a sudden flow discharge experiment at a higher flow velocity was performed, Reynolds\m 2.6x10^6. The transient evolution of the mean flow

properties, massflow, P_0, T_0 and inlet free stream axial flow velocity are represented in **Figure 22**. Figure 26 depicts the wall pressure distribution along the hump centerline for several time steps along the condition start-up. As the flow is set into motion, t>0.1 s, the hump imposes the flow expansion and diffusion across the centerline of the domain. Which is illustrated by the progressive reduction of static pressure towards the hump pinnacle. Driven by the sudden flow discharge the boundary layer is able to overcome the adverse pressure gradient and there is no presence of flow separation during the start-up, t<0.3 s. As the acceleration rate dilutes the boundary layer detaches and a plateau on the pressure evolution is noticed for t>0.35. The recirculated flow region gradually increases its extension up to its establishment, t > 0.4. Figure 27 illustrates the stream-wise velocity component deviation from the average local velocity. The transient local unsteadiness above the recirculated flow region depicts values in agreement with inlet turbulence level. Along the recirculated region when operating at nominal conditions the mean local unsteadiness is around 50 %, in agreement with the values obtained for the steady traverses under operation at $1.5x10^6$ and $2.6x10^6$.

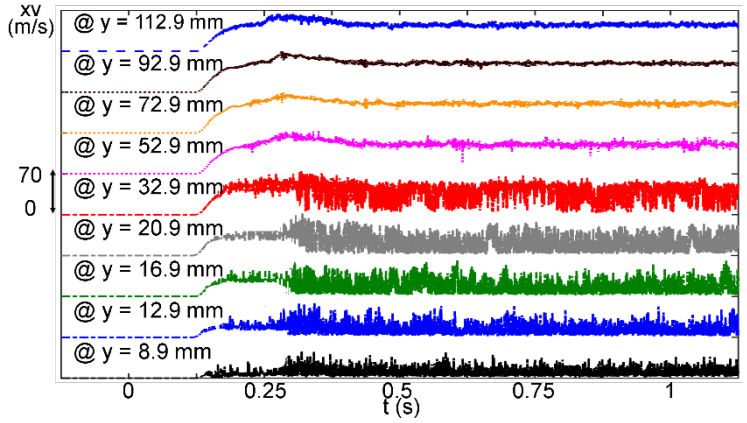

Figure 27: Stream-wise velocity transient evolution during $2.6x10^6$ sudden

However, during the initial phases of the sudden discharge, t < 0.3 s the local unsteadiness remains below 6 %. Indicating the absence of massive flow separation along the diffusion section of the hump. Which evidences the momentum boost received by the near wall flow region. Figure 28 represents the transient evolution of the stream-wise velocity component at various normal distances from the wall, 60 mm downstream of the hump summit. The mid-span velocity (y > 52.9 mm) display identical evolution, the flow accelerates following the arrival of the compression waves up to t = 0.3 s, where it reaches a maximum value and then gradually adjusts to the nominal operating condition, t >0.4 s.

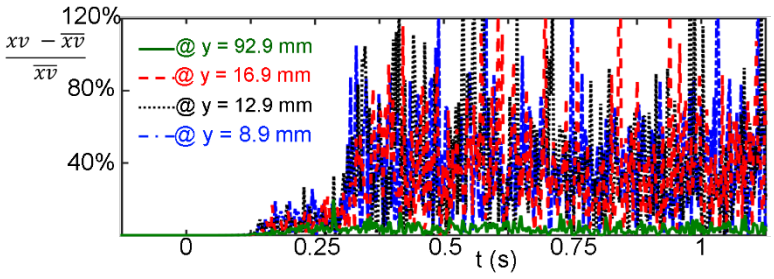

Figure 28: Local axial velocity unsteadiness during $2.6x10^6$ Sudden

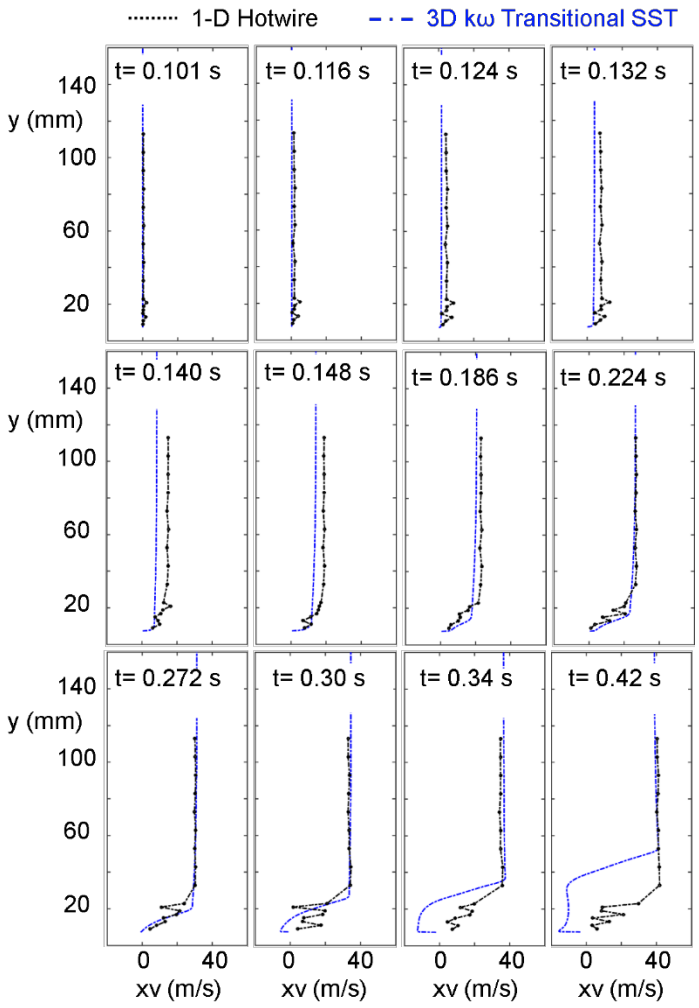

Figure 29: Stream-wise velocity profile at several time-steps along the sudden flow discharge 2.6x10^6, experimental profiles (1-D Hotwire) vs. URANS numerical prediction

Figure 29 represents the axial velocity profile across the height of the test section 60 mm downstream of the hump summit for several time steps along the transient. The experimental velocity profile is compared against the results of a 3D URANS blow-down simulation. The sudden flow discharge in the numerical simulation was imposed with a smoother-step profile evolution that mimicked the pressure rise over 100 ms. The use of a smoother step profile enhances the numerical stability of the simulation although it generates some disagreements on the initial release of pressure waves at the inlet. Following the arrival of the initial pressure waves the flow is set into motion t = 0.124 s. The numerical profile follows behind the initial flow acceleration, t < 0.186, due to the differences on the inlet total pressure prescription. However, for t > 0.186 the core flow velocity evolution is almost identical to the experimental one. The numerical blow down simulation reflects attached flow performance for t < 0.272 at the probe axial location. Similarly, the local unsteadiness in the experimental profile remains at moderate levels up to that point. Afterwards, for t >0.27 there is a portion of the velocity profile that reveals reversed flow performance in the numerical simulations and larger profile deviations in the experimental results. The growth of the reversed flow region extends above the region of larger unsteadiness and lower velocity magnitude monitored by the hotwire, as already illustrated for steady state performance in Figure 16 and Figure 17.

Conclusions

Transient flow behavior impacts momentum and thermal boundary layer development in all fluid-mechanic machinery. The near wall region can suffer from inertia, turbulence mitigation, or turbulence enhancement driven by sudden changes or oscillatory behavior of the free-stream conditions. This phenomenon is of particular relevance for short duration wind tunnels where the flow is set into motion by shock waves and only a few milliseconds of testing are available. In a similar way, the confined flow inside of turbomachinery passages or heat exchangers suffers from mean flow oscillations driven by upstream components. Free-stream flow changes, in particular sudden flow accelerations affect the development of the boundary layer and impact the evolution of the wall fluxes.

During transient flow conditions or periodic flow perturbations, the flow momentum near the wall region can be benefited from the unsteady flow behavior and delay or prevent the boundary layer detachment. The flow separation is induced by the lack of momentum on the near wall region when exposed to adverse pressure gradients. This dissertation analyzed the behavior of separated flows, reporting the inception and separation length, under non-temporally uniform inlet conditions through Unsteady Reynolds average Navier–Stokes (URANS), large Eddy simulations (LES) and experiments in a linear wind tunnel. The investigation is focused on ad-hoc wall mounted hump that mimics the performance of a low pressure turbine airfoil. Where the flow is attached for high Reynolds number but the boundary layer detaches for low Reynolds conditions. Through sudden flow accelerations, the dynamic response of the shear layer detachment was also assessed. While based on periodic inlet total pressure fluctuations the performance of flow separation under continuous flow oscillations was explored.

Based on the sudden flow discharge analysis, at similar Reynolds conditions, the presence of flow acceleration energizes the near wall flow preventing the flow separation. On the contrary, in case of mean flow deceleration, the boundary layer is more predisposed to detach and the length of the separated region increases. In this line, the strong influence of the mean flow temporal evolution on the separation onset was remarked. Under periodic disturbances, once the excitation rates approach the domain frequency response, the mean flow quantities tend to an average condition. However, the boundary layer flow can perceive the influence of the pressure and expansion waves propagating across the domain, modulating its reaction when exposed to adverse pressure gradients.

To assess experimentally the impact of mean flow transients on the flow detachment and reattachment process a modular wind tunnel tailored to fundamental and low technology readiness level, 1-2, was designed and commissioned. The working section, 70x230 mm cross section and 550 mm long, has full visual access and can operate in sub-atmospheric and over-pressure conditions. The test section is defined by windows, allowing complete imaging resolution and enabling the use of a myriad of optical techniques to characterize the near wall region. The test conditions in the working section can vary from Reynolds/m [1×10^5 - 1.9×10^8] and Mach [0.005 - 6.5]. The design of the flow conditioning system was optimized with 3D Unsteady Reynolds Average Simulations to guarantee its performance. Delivering uniform flow conditions with a minimal response time to the upstream flow changes. Taking advantage of this facility, aero-thermodynamic measurements over the designed wall mounted hump were carried out to monitor the temporal evolution of boundary layer detachment and reattachment. The inlet flow conditions to the test article were interrogated with total pressure, total temperature and hotwire traverses. The transient growth of the recirculated flow region under the mean flow transients was monitored by means of wall pressure readings and hotwire traverses. Driven by the sudden flow release, the near wall region can overcome the adverse pressure gradient. As the flow acceleration dilutes, the boundary layer detaches and the separated flow region grows. The experimental results are compared to 2D and 3D transient Computational Fluid

Dynamic simulations. Which proof the capability of Unsteady Reynolds Average Navier-Stokes models predicting the dynamics of this phenomena although over-predicting the extension of the separation.

Once the boundary layer detachment phenomena under mean flow transients was characterized, flow control strategies based on flow injection and absorption were analyzed. To investigate the impact of flow control on the flow separation dynamic response a slot was included in the geometry. Allowing the exploration of the recirculated flow region behavior under flow aspiration and injection. Low-frequency excitation effectively abates the flow separation near the actuation extremes. However, it fails to prevent separation along the mean levels of the actuation envelope. As the frequency of actuation increases, the cyclic injection-ingestion effectively prevents the separation onset throughout the entire period. In addition, the thermal and axial velocity profiles tend to an average status, which reduces the heat transfer rate from the core flow to the wall. The actuation performance is boosted when the actuator frequency matches the frequency response of the separated region.

References

[1] Stewartson, K. t., 1951, "On the impulsive motion of a flat plate in a viscous fluid," The Quarterly Journal of Mechanics and Applied Mathematics, 4(2), pp. 182-198.
[2] Stewartson, K., 1960, "The theory of unsteady laminar boundary layers," Advances in applied mechanics, 6, pp. 1-37.
[3] Rott, N., 1964, "Theory of time-dependent laminar flows," Princeton Univ. Press, Princeton, NJ, p. 421.
[4] Moore, F. K., 1951, "Unsteady laminar boundary-layer flow," No. NACA-TN-2471.
[5] Huang, H.-S., and Yang, W.-J., 1969, "Unsteady compressible laminar boundary-layer flow over a flat plate," AIAA Journal, 7(1), pp. 100-105.
[6] Schetz, J., and Oh, S. K., 1968, "Approximate Analysis of Transient Laminar Boundary-Layer Development," Journal of Heat Transfer, 90(4), pp. 452-456.
[7] Mirels, H., 1956, "Boundary layer behind shock or thin expansion wave moving into stationary fluid," NACA TN-3712.
[8] Mirels, H., 1958, "The wall boundary layer behind a moving shock wave," Grenzschichtforschung/Boundary Layer Research, Springer, pp. 283-293.
[9] Holden, M. S., 1971, "Establishment time of laminar separated flows," AIAA journal, 9(11), pp. 2296-2298.
[10] Holden, M. S., 1975, "Shock wave turbulent boundary layer interaction in hypersonic flow," DTIC Document.
[11] Lee, J.-Y., and Lewis, M., 1993, "Numerical study of the flow establishment time in hypersonic shock tunnels," Journal of Spacecraft and Rockets, 30(2), pp. 152-163.
[12] Davies, W., and Bernstein, L., 1969, "Heat transfer and transition to turbulence in the shock-induced boundary layer on a semi-infinite flat plate," Journal of Fluid Mechanics, 36(01), pp. 87-112.
[13] Smith, C. E., 1966, "The starting process in a hypersonic nozzle," Journal of Fluid Mechanics, 24(04), pp. 625-640.
[14] Lam, S.-H., and Crocco, L., 1958, Shock induced unsteady laminar compressible boundary layers on a semi-infinite flat plate, Princeton University.
[15] Horlock, J., and Evans, R., 1975, "The momentum-integral equation for a boundary layer with turbulence or ordered unsteadiness in the free stream," Journal of Fluids Engineering, 97(1), pp. 126-129.
[16] Touber, E., and Sandham, N. D., 2011, "Low-order stochastic modelling of low-frequency motions in reflected shock-wave/boundary-layer interactions," Journal of Fluid Mechanics, 671, pp. 417-465.
[17] Saavedra, J., Paniagua, G., and Lavagnoli, S., 2018, "On the transient response of the turbulent boundary layer inception in compressible flows," Journal of Fluid Mechanics, 850, pp. 1117-1141.
[18] Binder, A., Forster, W., Kruse, H., and Rogge, H., 1985, "An experimental investigation into the effect of wakes on the unsteady turbine rotor flow," Journal of Engineering for Gas Turbines and Power, 107(2), pp. 458-465.
[19] Arndt, N., "Blade row interaction in a multistage low-pressure turbine," Proc. ASME 1991 International Gas Turbine and Aeroengine Congress and Exposition, American Society of Mechanical Engineers, pp. V001T001A091-V001T001A091.
[20] Giles, M. B., 1988, "Calculation of unsteady wake/rotor interaction," Journal of Propulsion and Power, 4(4), pp. 356-362.

[21] Chaluvadi, V., Kalfas, A., Banieghbal, M., Hodson, H., and Denton, J., 2001, "Blade-row interaction in a high-pressure turbine," Journal of Propulsion and Power, 17(4), pp. 892-901.
[22] Moss, R. W., Ainsworth, R. W., and Garside, T., "Effects of rotation on blade surface heat transfer: an experimental investigation," Proc. ASME 1997 International Gas Turbine and Aeroengine Congress and Exhibition, American Society of Mechanical Engineers, pp. V003T009A034-V003T009A034.
[23] Braun, J., Saracoglu, B. H., and Paniagua, G., 2016, "Unsteady Performance of Rotating Detonation Engines with Different Exhaust Nozzles," Journal of Propulsion and Power, pp. 1-10.
[24] Paniagua, G., Iorio, M., Vinha, N., and Sousa, J., 2014, "Design and analysis of pioneering high supersonic axial turbines," International Journal of Mechanical Sciences, 89, pp. 65-77.
[25] Grönman, A., Turunen-Saaresti, T., Jaatinen, A., and Backman, J., 2010, "Numerical modelling of a supersonic axial turbine stator," Journal of Thermal Science, 19(3), pp. 211-217.
[26] Sousa, J., Paniagua, G., and Saavedra, J., 2017, "Aerodynamic response of internal passages to pulsating inlet supersonic conditions," Computers & Fluids, 149, pp. 31-40.
[27] Hasan, A. T., 2014, "Characteristics of overexpanded nozzle flows in imposed oscillating condition," International Journal of Heat and Fluid Flow, 46, pp. 70-83.
[28] Braun, J., Saavedra Garcia, J., and Paniagua, G., "Evaluation of the unsteadiness across nozzles downstream of rotating detonation combustors," Proc. 55th AIAA Aerospace Sciences Meeting, p. 1063.
[29] Lighthill, M., "On boundary layers and upstream influence. I. A comparison between subsonic and supersonic flows," Proc. Proceedings of the Royal Society of London A: Mathematical, Physical and Engineering Sciences, The Royal Society, pp. 344-357.
[30] Lighthill, M., "On boundary layers and upstream influence. II. Supersonic flows without separation," Proc. Proceedings of the Royal Society of London A: Mathematical, Physical and Engineering Sciences, The Royal Society, pp. 478-507.
[31] Lighthill, M., "Contributions to the theory of heat transfer through a laminar boundary layer," Proc. Proceedings of the Royal Society of London A: Mathematical, Physical and Engineering Sciences, The Royal Society, pp. 359-377.
[32] Uchida, S., 1956, "The pulsating viscous flow superposed on the steady laminar motion of incompressible fluid in a circular pipe," Zeitschrift für angewandte Mathematik und Physik ZAMP, 7(5), pp. 403-422.
[33] MIZUSHINA, T., MARUYAMA, T., and SHIOZAKI, Y., 1974, "Pulsating turbulent flow in a tube," Journal of Chemical Engineering of Japan, 6(6), pp. 487-494.
[34] Moschandreou, T., and Zamir, M., 1997, "Heat transfer in a tube with pulsating flow and constant heat flux," International journal of heat and mass transfer, 40(10), pp. 2461-2466.
[35] Saavedra, J., Lavagnoli, S., and Paniagua, G., "Implications of boundary layer establishment on convective heat transfer experiments," Proc. 53rd AIAA Aerospace Sciences Meeting, p. 0258.
[36] Poggie, J., "Compressible turbulent boundary layer simulations: resolution effects and turbulence modeling," Proc. 53rd AIAA Aerospace Sciences Meeting, pp. 6.2015-1983.
[37] Poggie, J., and Leger, T., 2015, "Large-scale unsteadiness in a compressible, turbulent reattaching shear layer," Experiments in Fluids, 56(11), p. 205.
[38] Ebert, D. S., Musgrave, F. K., Peachey, D., Perlin, K., and Worley, S., 2003, Texturing & modeling: a procedural approach, Morgan Kaufmann.
[39] Mullenix, N., Gaitonde, D., and Visbal, M., "A Plasma-Actuator-Based Method to Generate a Supersonic Turbulent Boundary Layer Inflow Condition for Numerical Simulations," Proc. 20th AIAA Computational Fluid Dynamics Conference, p. 3556.

[40] Bisek, N. J., Rizzetta, D. P., and Poggie, J., 2013, "Plasma control of a turbulent shock boundary-layer interaction," AIAA journal, 51(8), pp. 1789-1804.
[41] Poggie, J., Bisek, N. J., and Gosse, R., 2015, "Resolution effects in compressible, turbulent boundary layer simulations," Computers & Fluids, 120, pp. 57-69.
[42] White, F. M., and Corfield, I., 2006, Viscous fluid flow, McGraw-Hill New York.
[43] Elena, M., and Lacharme, J.-P., 1988, "Experimental study of a supersonic turbulent boundary layer using a laser Doppler anemometer," Journal de mécanique théorique et appliquée, 7(2), pp. 175-190.
[44] Alving, A. E., 1988, "Boundary layer relaxation from convex curvature."
[45] Konrad, W., 1993, "A three-dimensional supersonic turbulent boundary layer generated by an isentropic compression," PH. D. Thesis, Princeton University.
[46] Celik, I. B., Ghia, U., and Roache, P. J., 2008, "Procedure for estimation and reporting of uncertainty due to discretization in {CFD} applications," Journal of fluids {Engineering-Transactions} of the {ASME}, 130(7).
[47] Menter, F., Langtry, R., and Völker, S., 2006, "Transition modelling for general purpose CFD codes," Flow, turbulence and combustion, 77(1-4), pp. 277-303.
[48] Saavedra, J., Paniagua, G., and Chazot, O., 2018/08/10, "THERMAL BOUNDARY LAYER RESPONSE TO PERIODIC FLUCTUATIONS FOR TURBULENT FLOW," Journal of Engineering for Gas Turbines and Power.
[49] Spalart, P. R., 1986, "Numerical simulation of boundary layers. Part 3: Turbulence and relaminarization in sink flows."
[50] Launder, B. E., and Jones, W. P., 1969, On the prediction of laminarisation, HM Stationery Office.
[51] Marusic, I., Brandner, P., and Pearce, B., "The logarithmic region of wall turbulence: universality, structure and interactions," Proc. Proceedings of 18th Australasian Fluid Mechanics Conference, 3rd–7th December.
[52] Marusic, I., Monty, J. P., Hultmark, M., and Smits, A. J., 2013, "On the logarithmic region in wall turbulence," Journal of Fluid Mechanics, 716.
[53] Bons, J. P., Sondergaard, R., and Rivir, R. B., "The fluid dynamics of LPT blade separation control using pulsed jets," Proc. ASME Turbo Expo 2001: Power for Land, Sea, and Air, American Society of Mechanical Engineers, pp. V003T001A064-V003T001A064.
[54] Goldberg, C., Nalianda, D., Pilidis, P., MacManus, D., and Felder, J., "Installed performance assessment of a boundary layer ingesting distributed propulsion system at design point," Proc. 52nd AIAA/SAE/ASEE Joint Propulsion Conference, p. 4800.
[55] SHARMA, O., "Impact of Reynolds number on low pressure turbine performance," CP-1998-206958New York, USA: NASA, 1998: 65-70.
[56] Hura, H. S., Joseph, J., and Halstead, D. E., 2012, "Reynolds Number Effects in a Low Pressure turbine," ASME GT2012-68501.
[57] Gad-el-Hak, M., 1996, "Modern developments in flow control," Applied Mechanics Reviews, 49, pp. 365-380.
[58] Byerley, A. R., Störmer, O., Baughn, J. W., Simon, T. W., Van Treuren, K. W., and List, J. r., "Using gurney flaps to control laminar separation on linear cascade blades," Proc. ASME Turbo Expo 2002: Power for Land, Sea, and Air, American Society of Mechanical Engineers, pp. 1191-1199.
[59] Lake, J., King, P., and Rivir, R., "Reduction of separation losses on a turbine blade with low Reynolds numbers," Proc. 37th Aerospace Sciences Meeting and Exhibit, p. 242.

[60] Volino, R. J., 2003, "Passive flow control on low-pressure turbine airfoils," Transactions of the ASME-T-Journal of Turbomachinery, 125(4), pp. 754-764.
[61] Greenblatt, D., and Wygnanski, I. J., 2000, "The control of flow separation by periodic excitation," Progress in Aerospace Sciences, 36(7), pp. 487-545.
[62] Hultgren, L. S., and Ashpis, D. E., 2003, Demonstration of separation delay with glow-discharge plasma actuators, National Aeronautics and Space Administration, Glenn Research Center.
[63] Poggie, J., 2005, "DC glow discharges: a computational study for flow control applications," AIAA Paper, 5303, p. 2005.
[64] Roy, S., and Gaitonde, D. V., "Multidimensional collisional dielectric barrier discharge for flow separation control at atmospheric pressures," Proc. Proceedings 35th AIAA Fluid Dynamics Conference, pp. 6-9.
[65] Moreau, E., 2007, "Airflow control by non-thermal plasma actuators," Journal of physics D: applied physics, 40(3), p. 605.
[66] Huang, J., Corke, T. C., and Thomas, F. O., 2006, "Unsteady plasma actuators for separation control of low-pressure turbine blades," AIAA journal, 44(7), pp. 1477-1487.
[67] Göksel, B., Greenblatt, D., Rechenberg, I., Singh, Y., Nayeri, C., and Paschereit, C., 2006, "Pulsed plasma actuators for separation flow control," momentum, 10, p. 11.
[68] Porter, C., McLaughlin, T., Enloe, C., Font, G., Roney, J., and Baughn, J., 2007, "Boundary layer control using a DBD plasma actuator," AIAA paper, 786, p. 2007.
[69] Post, M. L., and Corke, T. C., 2004, "Separation control on high angle of attack airfoil using plasma actuators," AIAA journal, 42(11).
[70] Gaitonde, D. V., Visbal, M. R., and Roy, S., 2005, "Control of flow past a wing section with plasma-based body forces," AIAA paper, 5302, p. 2005.
[71] Rethmel, C., Little, J., Takashima, K., Sinha, A., Adamovich, I., and Samimy, M., 2011, "Flow separation control over an airfoil with nanosecond pulse driven DBD plasma actuators," AIAA paper, 487, p. 2011.
[72] Volino, R. J., 2003, "Separation control on low-pressure turbine airfoils using synthetic vortex generator jets," Transactions of the ASME-T-Journal of Turbomachinery, 125(4), pp. 765-777.
[73] Sondergaard, R., Rivir, R. B., and Bons, J. P., 2002, "Control of low-pressure turbine separation using vortex-generator jets," Journal of propulsion and power, 18(4), pp. 889-895.
[74] Schobeiri, M. T., Öztürk, B., and Ashpis, D. E., 2005, "On the physics of flow separation along a low pressure turbine blade under unsteady flow conditions," Journal of fluids engineering, 127(3), pp. 503-513.
[75] Wissink, J., 2003, "DNS of separating, low Reynolds number flow in a turbine cascade with incoming wakes," International Journal of Heat and Fluid Flow, 24(4), pp. 626-635.
[76] Seifert, A., and Pack, L. G., 2002, "Active flow separation control on wall-mounted hump at high Reynolds numbers," AIAA journal, 40(7), pp. 1363-1372.
[77] He, C., Corke, T. C., and Patel, M. P., 2007, "Numerical and experimental analysis of plasma flow control over a hump model," AIAA paper, 935, p. 2007.
[78] Pescini, E., Marra, F., De Giorgi, M., Francioso, L., and Ficarella, A., 2017, "Investigation of the boundary layer characteristics for assessing the DBD plasma actuator control of the separated flow at low Reynolds numbers," Experimental Thermal and Fluid Science, 81, pp. 482-498.
[79] Martínez, D., Pescini, E., Marra, F., De Giorgi, M., and Ficarella, A., "Analysis of the Performance of Plasma Actuators Under Low-Pressure Turbine Conditions Based on Experiments and URANS Simulations," Proc. ASME Turbo Expo 2017: Turbomachinery Technical

Conference and Exposition, American Society of Mechanical Engineers, pp. V02AT40A034-V002AT040A034.
[80] Kaiktsis, L., Karniadakis, G. E., and Orszag, S. A., 1991, "Onset of three-dimensionality, equilibria, and early transition in flow over a backward-facing step," Journal of Fluid Mechanics, 231, pp. 501-528.
[81] Barkley, D., Gomes, M. G. M., and Henderson, R. D., 2002, "Three-dimensional instability in flow over a backward-facing step," Journal of Fluid Mechanics, 473, pp. 167-190.
[82] Raverdy, B., Mary, I., Sagaut, P., and Liamis, N., 2003, "High-resolution large-eddy simulation of flow around low-pressure turbine blade," AIAA journal, 41(3), pp. 390-397.
[83] Curtis, E., Hodson, H., Banieghbal, M., Denton, J., Howell, R., and Harvey, N., 1997, "Development of blade profiles for low-pressure turbine applications," Journal of Turbomachinery, 119(3), pp. 531-538.
[84] Howell, R., Ramesh, O., Hodson, H., Harvey, N., and Schulte, V., 2001, "High lift and aft-loaded profiles for low-pressure turbines," Journal of Turbomachinery, 123(2), pp. 181-188.
[85] Dolling, D. S., 2001, "Fifty years of shock-wave/boundary-layer interaction research: what next?," AIAA journal, 39(8), pp. 1517-1531.
[86] Ganapathisubramani, B., Clemens, N., and Dolling, D., 2007, "Effects of upstream boundary layer on the unsteadiness of shock-induced separation," Journal of Fluid Mechanics, 585, pp. 369-394.
[87] Dussauge, J.-P., Dupont, P., and Debiève, J.-F., 2006, "Unsteadiness in shock wave boundary layer interactions with separation," Aerospace Science and Technology, 10(2), pp. 85-91.
[88] Schobeiri, M., and Ozturk, B., "Experimental study of the effect of periodic unsteady wake flow on boundary layer development, separation, and re-attachment along the surface of a low pressure turbine blade," Proc. ASME Turbo Expo 2004: Power for Land, Sea, and Air, American Society of Mechanical Engineers, pp. 247-265.
[89] Johnston, J. P., and Nishi, M., 1990, "Vortex generator jets-means for flow separation control," AIAA journal, 28(6), pp. 989-994.
[90] Huang, J., Corke, T. C., and Thomas, F. O., 2006, "Plasma actuators for separation control of low-pressure turbine blades," AIAA journal, 44(1), pp. 51-57.
[91] 1971, "Boundary layer control of flow separation and heat exchange," US Patent 3,578,264.
[92] Chun, K.-B., and Sung, H., 1996, "Control of turbulent separated flow over a backward-facing step by local forcing," Experiments in Fluids, 21(6), pp. 417-426.
[93] Jovic, S., and Driver, D., 1995, "Reynolds number effect on the skin friction in separated flows behind a backward-facing step," Experiments in Fluids, 18(6), pp. 464-467.
[94] Abe, K., Kondoh, T., and Nagano, Y., 1994, "A new turbulence model for predicting fluid flow and heat transfer in separating and reattaching flows—I. Flow field calculations," International journal of heat and mass transfer, 37(1), pp. 139-151.
[95] Dejoan, A., and Leschziner, M., 2004, "Large eddy simulation of periodically perturbed separated flow over a backward-facing step," International Journal of Heat and Fluid Flow, 25(4), pp. 581-592.
[96] Kim, J., Kline, S., and Johnston, J. P., 1980, "Investigation of a reattaching turbulent shear layer: flow over a backward-facing step," Journal of Fluids Engineering, 102(3), pp. 302-308.
[97] Biswas, G., Breuer, M., and Durst, F., 2004, "Backward-facing step flows for various expansion ratios at low and moderate Reynolds numbers," Journal of fluids engineering, 126(3), pp. 362-374.

[98] Kaiktsis, L., Karniadakis, G. E., and Orszag, S. A., 1996, "Unsteadiness and convective instabilities in two-dimensional flow over a backward-facing step," Journal of Fluid Mechanics, 321, pp. 157-187.
[99] Vogel, J., and Eaton, J., 1985, "Combined heat transfer and fluid dynamic measurements downstream of a backward-facing step," Journal of heat transfer, 107(4), pp. 922-929.
[100] Paniagua, G., Cuadrado, D., Saavedra, J., Andreoli, V., Meyer, T., Meyer, S., and Lawrence, D., "Design of the Purdue Experimental Turbine Aerothermal Laboratory for Optical and Surface Aero-Thermal Measurements," Proc. ASME Turbo Expo 2016: Turbomachinery Technical Conference and Exposition, American Society of Mechanical Engineers, pp. V006T005A025-V006T005A025.
[101] Saavedra, J., Paniagua, G., and Saracoglu, B., 2017, "Experimental Characterization of the Vane Heat Flux Under Pulsating Trailing-Edge Blowing," Journal of Turbomachinery, 139(6), p. 061004.
[102] Saavedra, J., Paniagua, G., and Chazot, O., 2019, "Thermal Boundary Layer Response to Periodic Fluctuations for Turbulent Flow," Journal of Engineering for Gas Turbines and Power, 141(3), p. 031009.
[103] Paniagua, G., Yasa, T., La Loma, A. D., Castillon, L., and Coton, T., 2008, "Unsteady strong shock interactions in a transonic turbine: experimental and numerical analysis," Journal of Propulsion and Power, 24(4), pp. 722-731.
[104] Langtry, R. B., and Menter, F. R., 2009, "Correlation-based transition modeling for unstructured parallelized computational fluid dynamics codes," AIAA journal, 47(12), pp. 2894-2906.
[105] Sod, G. A., 1977, "A numerical study of a converging cylindrical shock," Journal of Fluid Mechanics, 83(04), pp. 785-794.
[106] Martí, J. M., and Müller, E., 1994, "The analytical solution of the Riemann problem in relativistic hydrodynamics," Journal of Fluid Mechanics, 258, pp. 317-333.
[107] Sod, G. A., 1978, "A survey of several finite difference methods for systems of nonlinear hyperbolic conservation laws," Journal of computational physics, 27(1), pp. 1-31.
[108] Toro, E. F., Spruce, M., and Speares, W., 1994, "Restoration of the contact surface in the HLL-Riemann solver," Shock waves, 4(1), pp. 25-34.
[109] Saito, T., and Takayama, K., 1999, "Numerical simulations of nozzle starting process," Shock Waves, 9(2), pp. 73-79.

List of Symbols, Abbreviations and Acronyms

A	Area	[m^2]
c	Speed of sound	[m/s]
cf	Skin friction	[-]
C	Covariance	[-]
CCF	Cross Correlation factor	[-]
cd	Drag coefficient	[-]
cp	Heat capacity	[J/K]
d	Model order	[-]
δ	Boundary layer thickness	[m]
δ^*	Boundary layer displacement thickness	[m]
Δ	Increment	[-]
DBD	Dielectric Barrier Discharge	[-]
f	Frequency	[Hz]
FFT	Fast Fourier Transform	[-]
FSD	Flow Separation Domain	[-]
γ	Required precision	[-]
GCI	Grid Convergence Index	[-]
h	Domain height	[m]
HP	High Pressure	[-]
htc	Heat transfer coefficient	[W/m2K]
k	Acceleration parameter	[-]
kn	Number of independent variables	[-]
L	Length	[m]
LE	Leading Edge	[-]
LES	Large eddy simulations	[-]
LP	Low Pressure	[-]
M	Mach number	[-]
μ	Dynamic Molecular viscosity	[kg/(ms)]
ν	Kinematic Molecular Viscosity	[-]
N	Contraction Ratio	[-]
θ	Boundary layer momentum thickness	[m]
P	Pressure	[Pa]
p	Period	[-]
PETAL	Purdue Experimental Turbine Aerothermal Laboratory	[-]
Pr	Prandtl number	[-]
$\dot{q}$	Heat flux rate	[W/ m^2]
RANS	Reynolds Average Navier Stokes	[-]
Re	Reynolds number	[-]
ρ	Density	[kg/ m^3]
RMS	Root Mean Square	[-]
RMSE	Root Mean Squared Error	[-]
RMSD	Root Mean Squared Deviation	[-]
σ	Standard deviation	[-]
SST	Shear Stress Transport	[-]
St	Strouhal number	[-]
τ	Wall Shear Stress	[Pa]
t	Time	[s]
T	Temperature	[K]

TE	Trailing Edge	[-]
TRL	Technology Readiness Level	[-]
Tu%	Turbulence Intensity	[-]
u	Free stream velocity	[m/s]
w	Wire	[-]
xv	Axial Velocity	[m/s]
x	Axial Distance	[m]
y	Normal distance	[m]

Subscripts and superscripts

Subscripts

0	Stagnant
ax	Axial
dyn	Dynamic
exc	Excitation
o	Obstacle
r	Reattachment
ref	Reference
th	Thermal
∞	Free stream conditions\
$\bar{}$	Massflow Averaged

Superscripts

+	Wall Units
*	Observation location

Appendix, Uncertainty Evaluation

In order to quantify the uncertainty of the measurements all primary variables used in their derivation factors are taken into account. The main sources of uncertainty in the methodology are summarized in Table 5. All error evaluations are given at 95% confidence level.

The absolute uncertainty of each derived quantity is estimated based on the variable mean value and impact of the uncertainty of each one of the prime factors used to derive that quantity. For example, Table 6 represents the Venturi massflow uncertainty. The massflow through the critical Venturi depends only on 3 prime variables: total pressure, total temperature and discharge coefficient (obtained from Venturi calibration). Based on the mean value for each one of these quantities the mean massflow is obtained. Then additional evaluations of the massflow computation are repeated including the uncertainty of each one of the prime variables. Considering the mean value of the total pressure plus its uncertainty the massflow is re-evaluated keeping the other quantities at its mean value. The outcome of that calculation reflects the massflow uncertainty associated to the total pressure uncertainty reading. The same procedure is repeated for each one of the prime variables and the global uncertainty is the square root of the sum of squares of the individual uncertainties. Finally, the sensitivity of the derived variable to each one of the independent variables can also be obtained when dividing the outcome variation by the original independent absolute uncertainty. Similar procedures are followed for the uncertainty derivation on Reynolds number, Table 7; flow velocity derived from P0, T0 and P, Table 19; hotwire flow velocity, Table 20; heat flux, Table 21; and heat transfer coefficient, Table 22.

Table 5: Transducers s absolute uncertainty

Variable/Sensor	Uncertainty	Unit
Venturi T	1	K
Venturi Pressure	1723	Pa
Test Section Pressure	50	Pa
Test Section T	0.3 %	
Venturi Calibration c_f	0.0178	
hotwire Voltage	10^{-4}	V
hotwire α	0.001	

Table 6: Massflow uncertainty

	Mean #	Unit	Abs. Uncer.	$\dot{m}$ with Uncer.	$\Delta\dot{m}$ (%)	Sensitivity
P_0	626328	Pa	1723	1.52	0.28	100.1
T_0	270	K	1	1.51	0.19	50.0
c_f	1		0.0178	1.54	1.78	100.0
$\dot{m}$	1.51	kg/s			1.50	

Table 7: Reynolds uncertainty

	Mean #	Unit	Abs. Uncer.	Re with Uncer.	ΔRe (%)	Sensitivity
P_0	101885	Pa	50	1148340	4.38	8922
P	11325	Pa	50	1050066	4.55	9228
T_0	275	K	1	1095043	0.47	128.1
Re	1100168				3.07	

Table 19: Stream-wise velocity uncertainty

	Mean #	Unit	Abs. Uncer.	xv with Uncer.	ΔRe (%)	Sensitivity
P_0	101885	Pa	50	30.11	2.12	4325
P	11325	Pa	50	28.96	1.78	3602
T_0	275	K	1	29.54	0.18	49.95
xv	29.48	m/s			2.77	

Table 20: Hotwire stream-wise velocity uncertainty

	Mean #	Unit	Abs. Uncer.	xv with Uncer.	ΔRe (%)	Sensitivity
P_0	100598	Pa	50	33.48	0	0
P	99674	Pa	50	33.47	0.03	59.98
T_0	283.62	K	1	33.60	0.37	2.09
$_{Wire}\Omega$	13.10	Ω	0.01	33.44	0.11	140.62
α_h	$9x10^{-4}$	1/K	$5\ 10^{-5}$	34.93	0.11	1.93
V	0.72	V	10^{-3}	33.48	0.00	21.83
n_h	0.71		$2.6\ 10^{-3}$	31.79	5.04	131.86
A_h	$5.2x10^{-7}$		$2.0\ 10^{-8}$	31.77	5.11	134.93
xv	33.48	m/s			7.19	

Table21: Heat flux calculation uncertainty

	Mean #	Unit	Abs. Uncer.	$\dot{q}$ with Uncer.	$\Delta\dot{q}$ (%)	Sensitivity
Al d	0.05	m	$2x\ 10^{-4}$	5745.4	0.01	2.86
Al κ	180	W/(mK)	7.2	5758.3	0.21	5.31
Al ρ	2700	Kg/m^3	100	5755.5	0.16	4.43
Al c_p	897	J/(kgK)	10	5748.7	0.05	4.43
c_k d	$4x10^{-4}$	m	$5\ x10^{-5}$	6214.4	8.15	65.20
c_k κ	1.3	W/(mK)	0.1	6031.7	4.97	64.56
c_k ρ	1335.98	Kg/m^3	45	5751.2	0.09	2.66
c_k c_p	990	J/(KgK)	25	5750.1	0.07	2.77
T_{wall}	340	K	1.5	5750.1	0.07	161
$\dot{q}$	5746.1	W/m^2			9.55	

Table 22: Heat transfer coefficient uncertainty

	Mean #	Unit	Abs. Uncer.	htc_{aw} with Uncer.	Δhtc (%)	Sensitivity
Al d	0.05	m	$2x\ 10^{-4}$	83.45	0.01	2.86
Al κ	180	W/(mK)	7.2	83.63	0.21	5.31
Al ρ	2700	Kg/m^3	100	83.59	0.16	4.43
Al c_p	897	J/(kgK)	10	83.49	0.05	4.43
c_k d	$4x10^{-4}$	m	$5\ x10^{-5}$	90.26	8.15	65.20
c_k κ	1.3	W/(mK)	0.1	87.60	4.97	64.56
c_k ρ	1335.98	Kg/m^3	45	83.53	0.09	2.66
c_k c_p	990	J/(KgK)	25	83.51	0.07	2.77
T_{wall}	340	K	1.5	81.41	2.45	556.42
htc_{aw}	83.45	$W/(m^2K)$			9.86	